Experimental Designs for Efficient Free-Space Multi-Spatial-Mode Optical Communication

by

Edwin Ng

Submitted to the Department of Physics
in partial fulfillment of the requirements for the degree of

Bachelor of Science in Physics

at the

MASSACHUSETTS INSTITUTE OF TECHNOLOGY

June 2013

© Edwin Ng, 2013. All rights reserved.

The author hereby grants to MIT permission to reproduce and to distribute publicly paper and electronic copies of this thesis document in whole or in part in any medium now known or hereafter created.

Author . . . .
Department of Physics
May 29, 2013

Certified by . . . .
Franco N.C. Wong
Senior Research Scientist
Thesis Supervisor

Accepted by . . . .
Nergis Mavalvala
Senior Thesis Coordinator, Department of Physics

Experimental Designs for Efficient Free-Space Multi-Spatial-Mode Optical Communication

by

Edwin Ng

Submitted to the Department of Physics
on May 29, 2013, in partial fulfillment of the
requirements for the degree of
Bachelor of Science in Physics

Abstract

In optical communications, two measures of efficiency are commonly at odds. The first is the photon information efficiency (in bits/photon) which measures the information that each detected photon conveys; the second is the spectral efficiency (in bits/s/Hz) which measures the bit rate achieved under limited bandwidth.

One interesting communication protocol which can simultaneously obtain high information efficiency without sacrificing spectral efficiency, however, is spatial pulse-position-modulation (spatial-PPM), in which information is encoded into the spatial modes of light and sent through free space between transmitter and receiever.

This thesis aims to lay the groundwork for an experimental design to achieve efficient spatial-PPM free-space optical communication using 1550 nm light at the single photon level. We focus on presenting and evaluating a transmitter-receiever design by giving a precise characterization of its operation, properties, and limitations.

Thesis Supervisor: Franco N.C. Wong
Title: Senior Research Scientist

Acknowledgments

The context for the work contained in this thesis is the PIECOMM (Photon Information Efficient Communication) collaboration between MIT and Raytheon BBN Technologies. Work on this project started in 2011 with the experimental effort headed by Dr. Franco Wong, Dr. Valentina Schettini, and Shankari Rajagopal. I joined the project in June 2012 after Valentina and Shankari left, working under the supervision of Franco and Dr. Zheshen Zhang, who will continue with the project to its completion expected in late 2013, following my graduation from MIT.

Much of what is presented in this thesis—especially in experimental motivation, optical design, and project direction—is the result of what I have picked up and learned from Franco, between our one-on-one weekly discussions and the occasional PIECOMM team meetings. It is his guidance that has provided me with a manageable and clear direction to pursue in this project.

As an undergraduate working on essentially my first real experimental project, I also owe a large debt of gratitude to everyone on the experimental side of the Optical and Quantum Communications group, whose mentorship was my sole reliance for gaining competence in optics work. As my postdoctoral supervisor, Zheshen showed me everything from mounting lenses to data analysis. Veronika Stelmakh was the one who took my drawings and actually machined the optical switch housing at the Edgerton Student Shop. When several fibers on an optical switch broke, Tian Zhong sat down and showed me how to use the fiber splicer; he also has a way of inspiring me to find solutions to the most notorious problems. On the theory side, the first chapter of this thesis has benefited from discussions with Nivedita Chandrasakeran.

Additionally, Francesco Bellei, Adam McCaughan, and Qingyuan Zhao (Nanjing University) from Prof. Karl Berggren's Quantum Nanostructures and Nanofabrication group at RLE were our main collaborators for the early SNSPD coupling experiment described in Section 6.4. The long nights I spent with them aligning optics in their lab formed quite a unique experience.

This research opportunity was one of many made accessible to MIT undergraduates through the UROP program, whose financial and logistical support I worked under for both the summer and fall of 2013. The research activity in RLE has exposed me to ideas and concepts beyond the physics curriculum and the scope of my own project, forming a central component of my overall education at MIT.

The PIECOMM project is supported by DARPA under the InPho (Information in a Photon) program.

Contents

1 **Introduction** **13**

1.1 Information Efficiency vs. Spectral Efficiency 14

1.2 Multi-Spatial-Mode Optical Communication 15

1.3 Experimental Goals and Thesis Overview 16

2 **Basic Design and Optical Layout** **19**

2.1 Schematic Overview 19

2.2 The Focused-Beam Configuration 20

3 **Transmitter Design and Setup** **25**

3.1 Transmitter-side Optics 25

3.2 Generating Multiple Spatial Modes 27

3.3 Laboratory Setup for Transmitter Optics 32

4 **Transmitter Interface and Control** **37**

4.1 Voltage Profiles for Optical Switching 37

4.2 Power Balance and Control 39

4.3 LabVIEW Interface Programs 42

5 **Receiver Design and Setup** **51**

5.1 Receiver-side Optics 51

5.2 Laboratory Setup for Receiver Optics 53

5.3 Single Photon Free-Space Detectors 55

6 Characterization of Optical System 59

6.1 Leakages in Active Switching 60

6.2 CCD Imaging of Spatial Crosstalk 62

6.3 Tight-packing Crosstalk 65

6.4 Free-space Coupling Experiment 68

7 Conclusions 71

A CCD Camera Crosstalk Data 73

List of Figures

1-1 Focused-beam spatial modes and a spatial-PPM sequence 15

2-1 High-level overview of the experimental layout 19
2-2 Focused-beam propagation from transmitter to receiver 21
2-3 An aperture inefficient collimated beam configuration 22

3-1 Transmitter-side optics for the focused-beam configuration 26
3-2 Schematic of setup for 16 optical channel focused-beam source 28
3-3 Photograph of lab setup for the multi-spatial-mode source 31
3-4 Simulation for lab transmitter setup 33
3-5 Imaged beam profiles in transmitter optics 34
3-6 Photograph of lab setup for transmitter optical setup 35

4-1 Voltage profiling fits to voltage scans on 1 × 8 switch 39
4-2 Photograph of electronic control setup for active switching 43
4-3 Screenshot of `Double Channel Select.vi` interface 44
4-4 Screenshot of `Double Channel Dynamic.vi` interface 45
4-5 Cartoon of dynamic driving waveform for message encoding 46
4-6 Voltage waveform and optical response for symbol modulation 47
4-7 Reduced channel isolation at 10 kHz modulation rate 48

5-1 Receiver-side optics for the focused-beam configuration 52
5-2 Simulation for lab receiver setup 54
5-3 Imaged beam profiles in receiver optics 54
5-4 Beam scanner profiles at detector focal plane 55

5-5 Photograph of lab setup for receiver optical setup 56

6-1 Reference grid and integration superpixels for CCD imaging 62
6-2 CCD image of symbol CH(6,3) on linear and log grayscale 63
6-3 Relative channel powers on CH(6,3) by CCD imaging 64
6-4 Diffuse power at CCD array for unblocked beams 65
6-5 FB modes imaged with various α values 66
6-6 Grid and superpixels for tight-packed CCD imaging 66
6-7 Tight-packed symbol CH(6,3) on linear and log grayscale 67
6-8 Log-scale superpixel matrix for tight-packed symbol CH(6,3) 67
6-9 Source-detector channel correlations in free-space coupling 69

A-1 CCD imaged channel crosstalk data, at microlens array 74
A-2 CCD imaged channel crosstalk data, tight-packing 75

List of Tables

3.1 Channel layout and designations for free-space array 30
3.2 Switch fiber connections to free-space array 31

4.1 Voltage profiles for 1 × 8 switches 38
4.2 Channel transmissivity in 1 × 8 switches 40
4.3 Profile for 1 × 2 switch power balancing 41
4.4 Analog BNC connections to switching inputs 42

6.1 Power leakages in 1 × 8 switches 61

Chapter 1

Introduction

In *optical communication*, information is transmitted via light by encoding it onto the various physical properties of light, such as frequency, polarization, spatial mode, pulse position, and so on. As demonstrated by modern fiber-optics-based telecommunications, such protocols using light can achieve data rates significantly higher than is possible on traditional radio frequency protocols, which are limited by low bandwidth and electromagnetic interference.

Furthermore, optical communication has the advantage of maintaining these high data rates even in regimes of very low power, as the recent development of fast, high efficiency single photon detectors has enabled reliable communication down to the single photon level, in which the information is encoded onto individual photons. In some sense, this regime of optical communication addresses a very fundamental physical question: what is the information capacity of a photon?

Presently, most high data rate applications in optical communication utilize fiber to establish optical links, which, although a reliable and well-developed technology, is limited to a single spatial channel and to using many photons per bit. An alternative method, however, is *free-space optical communication* (FSO), in which light is propagated from transmitter to receiver through line-of-sight free space with few to no optical equipment in between. This can range from propagation through kilometers in atmosphere for terrestrial applications to hundreds of thousands of kilometers in interstellar medium for deep-space optical links.

The work in this thesis is dedicated towards the development of a feasible protocol for low power, efficient free-space optical communication by encoding information into the spatial modes of light. This approach is motivated by the desire for FSO protocols that can achieve high data rates even in regimes of low power and low bandwidth.

1.1 Information Efficiency vs. Spectral Efficiency

The two measures of efficiency that are relevant to these requirements are the *photon information efficiency* (PIE) and the *spectral efficiency* (SE). PIE for a given scheme is measured in units of bits/photon, which is the amount of information per photon received. SE, on the other hand, is measured in units of bits/sec/Hz, which is the bit rate per unit of bandwidth used.

As an example of how these quantities work, consider a simple time-based *pulse position modulation* (PPM) protocol: we send a symbol consisting of 1024 time bins, of which one contains a photon. The arrival of a photon therefore carries $\log_2 1024 = 10$ bits of information, and the PIE for time-based PPM is 10 bits/photon.

The bit rate, on the other hand, depends on the number of symbols (or photons) we send per unit time. Suppose we send 10^8 symbols per second, which means a symbol rate of 100 MHz. The bit rate is $\log_2 1024 \cdot 100\,\mathrm{MHz} = 1\,\mathrm{Gbps}$. However, the bandwidth utilized is given by the reciprocal of the size of our time bins, or $1024 \cdot 100\,\mathrm{MHz}$. This calculation results in a SE of only $1\,\mathrm{Gbps}/(1024 \cdot 100\,\mathrm{MHz}) \approx 0.01$ bits/s/Hz for time-based PPM.

Thus, while it is apparent how to obtain extremely high PIE in time-based PPM protocols, the SE suffers as a trade-off; in this case, the SE decreases exponentially with the PIE. Conversely, there are coherent detection schemes which can achieve high SE, but whose PIE is fundamentally limited to only a few bits/photon[1]. Even when we model the communication protocol as a bosonic channel to invoke the quantum-mechanical nature of single photons (replacing the Shannon capacity limit with the Holevo capacity limit), the trade-off between PIE and SE remains[2].

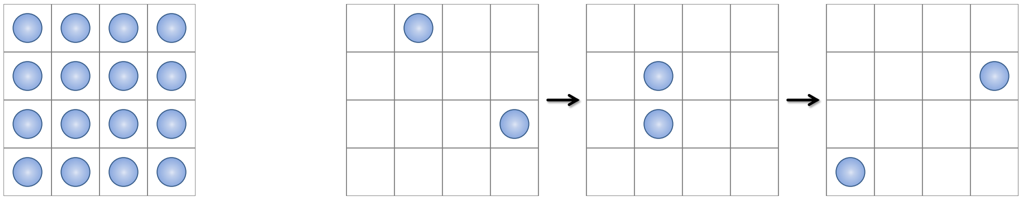

(a) The FB grid pattern (b) A sequence of spatially modulated FB grid symbols

Figure 1-1: Focused-beam spatial modes and a spatial-PPM sequence
Here, we represent 16 FB modes by arranging them in a 4×4 grid. To modulate, we use a 2-spatial-PPM scheme, where two pulses (one from the top half and one from the bottom half) are turned on at a time, giving 64 symbols.

1.2 Multi-Spatial-Mode Optical Communication

This problem can be avoided by making use of multiple spatial modes. In this experiment, we represent the spatial information of light in an intuitive way: as a grid of individual coherent Gaussian beams, such as that shown in Figure 1-1a. (For details on the properties of Gaussian beams and their propagation, consult [3] and [4].)

The spatial modes in this representation are called *focused-beam* (FB) modes. At their focal plane, the individual beams are small and spatially distinguished by their grid locations. Outside the focal plane, these beams can overlap one another, but they propagate along their individual wave vectors and can be distinguished when refocused. FB modes are convenient to work with because we need only a source of multiple *optical channels*, each carrying a single beam in, say, an optical fiber. We can then align the optical channels to output to free space in a grid formation and turn the channels on and off to perform modulation, as shown in Figure 1-1b.

Consider nowh a *spatial pulse position modulation* (spatial-PPM) scheme, in which we send light in, say, one of 1024 spatial FB modes (or channels). A symbol is the arrival of a photon in one of these spatial modes, so we have a PIE of 10 bits/photon just as before. Suppose we again send symbols at a rate of 100 MHz, giving a bit rate of 1 Gbps. The bandwidth in this scheme, however, is only 100 MHz, which results in a SE of 10 bits/s/Hz, which is three orders of magnitude higher than the original, time-based PPM protocol. Of course, this improvement requires the construction of a complex system for handling hundreds or even thousands of spatial channels.

In theory, for the low diffraction-loss vacuum-propagation bosonic channel where each spatial mode has the same transmissivity, the theoretical Holevo limits allows for general multi-spatial-mode FSO at 10 bits/photon and 5 bits/s/Hz with 189 spatial modes[1]. Realistically, it is not known how to build detectors that realize these theoretical limits, and suboptimal detection schemes like single photon counting are more practical. *On-off keying* (OOK) direct detection, where a photon is either detected in a spatial mode or not for each symbol, can reach these same PIE and SE values using approximately 4500 spatial modes[2].

The relevant distance scales L for multi-spatial-mode FSO are those in which the Fresnel number product $F = (D_T D_R/\lambda L)^2 \gg 1$, where D_T and D_R are the diameters of the transmitter and receiver apertures. For 1550 nm light, taking L to be tens of kilometers requires aperture diameters on the order of meters, essentially our upper limit. As a result, applications of multi-spatial-mode FSO will be mostly constrained to terrestrial communication through these distances. When the condition $F \gg 1$ is met, however, the maximum number of spatial modes (FB or otherwise) that can transmitted over the distance L is approximately F[2].

1.3 Experimental Goals and Thesis Overview

Given these theoretical considerations, the ultimate experimental goal is to design, implement, and test an experimental setup to achieve efficient multi-spatial-mode FSO with OOK direct detection, in a DARPA-funded project. This requires:

- the design of a system capable of transmission and detection of single photons in multiple spatial modes;
- the characterization of losses, noise, and crosstalk, and the design of error-correcting codes to address these errors;
- the ability to dynamically control the system at moderate symbol rates and implement the error-correction algorithms; and
- the assessment of the efficiencies of the setup relative to theoretical predictions.

The project goal is to build a proof-of-concept demonstration experiment which incorporates all of these experimental aspects and is furthermore scalable to more spatial modes, higher modulation speeds, and longer propagation distances.

The work documented in this thesis is meant to lay the groundwork for such a demonstration experiment taking place in the near-term. In particular, this thesis focuses on evaluating the transmitter-receiver design by giving a precise characterization of its operation, properties, and limitations.

We begin with a general schematic overview of the system in Chapter 2, where we establish a suitable optical configuration for working with multiple FB spatial modes. The experimental design for the transmitter system is described in detail in Chapter 3. Chapter 4 follows up on this discussion by investigating the operation of the switching elements for spatial and temporal modulation.

Meanwhile, Chapter 5 describes the experimental design for the receiver end of the system. Finally, in Chapter 6, we characterize the entire optical system by quantifying channel leakages and beam crosstalk; we also discuss the results of an early experiment performed to assess the free-space coupling between source and detector.

Chapter 7 concludes by mentioning some topics for future work to extend the results in this thesis towards a scalable design.

Chapter 2

Basic Design and Optical Layout

This chapter describes the basic concepts and considerations behind the design used in this experiment to achieve FB multi-spatial-mode FSO. We begin with a high-level overview of the optical layout and electronic signal chain. We then proceed to describe the input and output requirements of the transmitter and receiver designs for the focused-beam configuration. We want to think of the design in terms of modules, so we mostly defer specific implementation details to Chapters 3 and 5.

2.1 Schematic Overview

A schematic overview of the overall experimental design is shown in Figure 2-1 below, showing the fundamental modules in the design, namely: source/encoder, transmitter output, channel, receiver input, and detector/decoder.

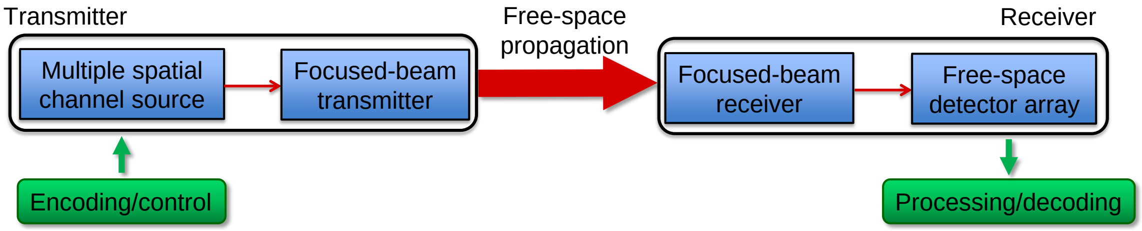
Transmitter
Multiple spatial channel source
Focused-beam transmitter
Free-space propagation
Receiver
Focused-beam receiver
Free-space detector array
Encoding/control
Processing/decoding

Figure 2-1: High-level overview of the experimental layout
The optical path is colored with red horizontal arrows, while the electronic control/signal paths are colored with green vertical arrows.

On the transmitter side, the *multiple spatial channel source* consists of a laser and a series of active switching elements. The laser generates fiber-coupled, single-mode light at 1550 nm. This output is connected by fiber to a number of active switching elements which split the laser light into one of multiple spatial channels (i.e., multiple fiber outputs). These spatial channels become FB spatial modes once the fibers are coupled to free space with a microlens array, giving a grid of parallel, spatially-separated beams. The switching elements are controlled by a computer, which acts as the encoder by performing the spatial and temporal modulation needed to encode messages. After the FB spatial modes are set up, they pass through a series of passive optical elements that make up the *focused-beam transmitter*. These elements prepare the light for transmission to the detector according to the focused-beam configuration as described in Section 2.2.

At the receiver, arriving light is collected by a series of passive optical elements (the *focused-beam receiver*) and manipulated to hit a *free-space detector array*, which registers the spatial location of the arriving light at its focal plane and sends that information to a computer for processing and decoding.

2.2 The Focused-Beam Configuration

In this section, we describe the form that the FB modes take in propagating through the free-space region from the transmitter output lens (*transmitter aperture*) to the receiver input lens (*receiver aperture*), as shown in Figure 2-2. We call this transmitter-receiver setup for handling FB modes the *focused-beam configuration*.

The beams start large and overlapping at the transmitter aperture, with their centers coinciding. However, by setting a slightly different initial angle for each beam, we can cause them to arrive at the receiver aperture with some center-to-center separation d_R after a propagation distance L. In addition, the lens located at the transmitter aperture causes the large beams to begin contracting, and by picking the transmitter aperture spot size w_T appropriately, it is possible to cause the beams to focus exactly at the receiver aperture with beam waist w_R, after free-space propagation through L.

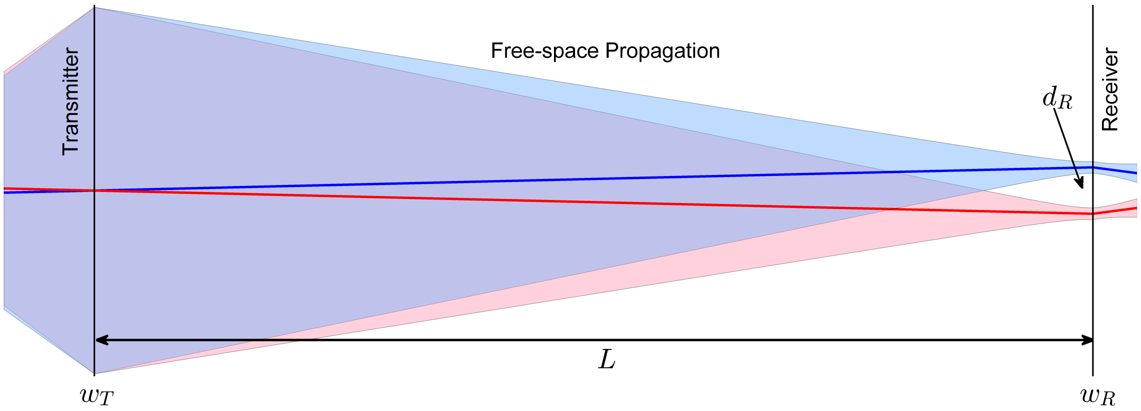

Figure 2-2: Focused-beam propagation from transmitter to receiver
This figure illustrates the principal features of two FB modes (colored blue and red) as they progagate through the free-space distance L from transmitter to receiver, showing the light ray and Gaussian envelope for each beam. The vertical black lines represent the transmitter and receiver apertures, where the beam waists are w_T and w_R, respectively. The beam separation at the receiver is d_R. The lenses and other optical elements needed to achieve this configuration are not shown.

At the receiver aperture, once the beams have focused and separated, the spatial information is available as individual beam positions. However, because the beams come in at an angle, we require additional optics to set the beams parallel again, as well as resize them to match the detector array dimensions.

An important fact about FB modes in general is that at their focal plane, the ratio α between the beam separations and the beam waists has an upper limit, as long as we use passive bulk optics (acting on all beams at once). Suppose that at some focal plane where the beams are parallel, the center-to-center distance of two adjacent beams in the grid pattern is d_0, while the beam waist is w_0, giving a ratio of $\alpha_0 = d_0/w_0$. Then at *any* other point of the optical path with corresponding dimensions d and w, $\alpha = d/w \leq \alpha_0$. Equality is obtained at a focal plane in which the beams are parallel. We call this maximum α_0 the *packing ratio*; it is set by the coupling from fiber to free-space in the multiple spatial channel source.

Perhaps it might be objected that the setup in Figure 2-2 looks asymmetric and that a more intuitive design might be to use parallel, collimated beams such as those shown in Figure 2-3. However, we can easily show that this "collimated beam configuration" of handling FB modes is much less aperture efficient.

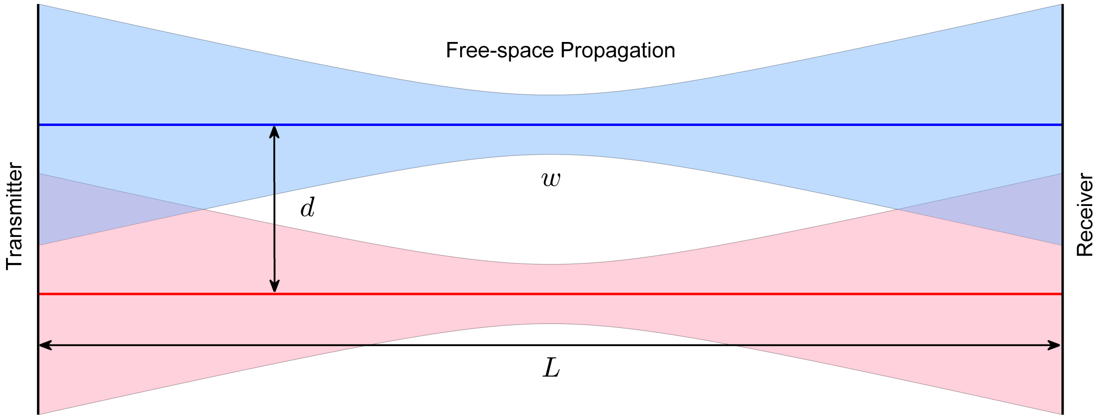

Figure 2-3: An aperture inefficient collimated beam configuration
An alternative to Figure 2-2, showing the same features but with parallel, collimated beams separated by d. Here, the beam waist w is chosen such that the distance L is equal to the confocal parameter, so that the beams are well-collimated throughout.

Suppose we try to send N spatial modes from transmitter to receiver. We can show that the aperture sizes D_T and D_R required are much greater for the collimated beam configuration than for the focused-beam configuration. We assume square apertures since the grid pattern is square, but this in turn dictates the lens diameters.

Because the beams are well-collimated throughout the propagation, L must be on the order of the confocal parameter, which gives

$$L \simeq \frac{2\pi w^2}{\lambda} \quad \Rightarrow \quad w \simeq \sqrt{\frac{\lambda L}{2\pi}}.$$

Consider now the focal plane at the halfway point. The beam separation d must be related to the beam waist by the packing ratio, so $d = \alpha_0 w$. Using parallel beams requires that $D_R = D_T \simeq \sqrt{N} \cdot d$. We therefore arrive at the conclusion that the product of the aperture diameters obeys

$$\frac{D_T D_R}{\lambda L} \simeq \frac{\alpha_0^2}{2\pi} \cdot N \quad \Rightarrow \quad N \propto \sqrt{F}. \tag{2.1}$$

Thus, the number of spatial modes achieved scales as $\sqrt{F}$, but F is the theoretical maximum number of spatial modes that can be transmitted, so the collimated beam configuration is suboptimal in aperture efficiency.

On the other hand, consider the focused-beam configuration. Recall that w_R and w_T are the beam sizes at the receiver and transmitter, respectively. If we try to pack N spatial modes into the receiver aperture, we find that

$$N(\alpha_0 w_R)^2 \simeq D_R^2 \quad \Rightarrow \quad w_R \simeq \frac{D_R}{\alpha_0\sqrt{N}}.$$

In the focused-beam configuration, L is considerably larger than the confocal parameter, so we can use the full divergence angle $\Theta = 2\lambda/\pi w_R$ to calculate the beam diameter at the transmitter: $2w_T \approx \Theta L$. All the beams overlap at the transmitter aperture, so its diameter is set by $2w_T$. We therefore get

$$\frac{D_T D_R}{\lambda L} \simeq \frac{2\alpha_0}{\pi} \cdot \sqrt{N} \quad \Rightarrow \quad N \propto F. \tag{2.2}$$

Compared to Equation 2.1, this is a quadratic improvement. Furthermore, Equation 2.2 shows that the number of FB modes achieved scales as F, the theoretical maximum. Hence, for α_0 not too large, the focused-beam configuration is asymptotically optimal in aperture efficiency.

Nevertheless, aperture efficiency is not the main concern of this experiment; we are interested much more in PIE and SE for fixed N. As a result, even though we could gain a small improvement in aperture efficiency with *tight packing* where $\alpha_0 \approx 1$, we avoid putting our beams so close together due to issues like crosstalk at the detector (see Section 6.3). When N is fixed, high detector crosstalk induces error-correction overhead, which can lower the PIE.

Chapter 3

Transmitter Design and Setup

This chapter describes the transmitter design for the experimental setup used in this thesis. We start by giving the transmitter-side optics that meet the input and output requirements imposed by the focused-beam configuration. We then look at the active switching elements which implement the multiple channel source, including the free-space coupling of the optical channels to create FB modes. Finally, we describe an experimental realization of the focused-beam transmitter and report on its performance against the design.

3.1 Transmitter-side Optics

In designing the transmitter-side optics, we need to consider its input and output constraints. On the input, suppose we have a source of multiple spatial channels which produces spatially separated, parallel beams, fixing an initial focal plane where the beams have waists w_0 and grid separations d_0 (with packing ratio $\alpha_0 = w_0/d_0$).

At the same time, the receiver end of the focused-beam configuration requires the transmitter optics to output centered, overlapping beams radius w_T and each with a different initial tilt. In particular, for a receiver aperture beam waist w_R, we need

$$w_T = w_R \sqrt{1 + L^2 \left(\frac{\lambda}{\pi w_R^2} \right)^2} \approx \frac{\lambda L}{\pi w_R}. \tag{3.1}$$

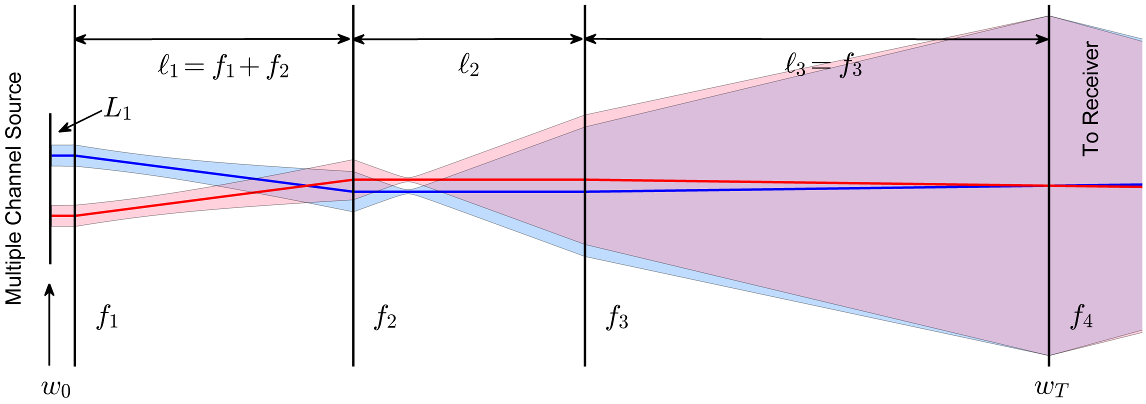

Figure 3-1: Transmitter-side optics for the focused-beam configuration
We show the propagation of two FB modes with initial beam waist w_0 at the multiple channel source focal plane and ending with beam radius w_T at the aperture. The four lenses are represented by vertical lines labelled f_1 through f_4. The length ℓ_2 is constrained in Equation 3.3. L_1 denotes the distance between the source focal plane and f_1. This setup combines with Figure 5-1 to implement the focused-beam configuration introduced in Figure 2-2.

To address these requirements, we use the transmitter optical design shown in Figure 3-1, which is composed of essentially two parts. The first, comprising lenses f_1 and f_2, is a telescope which shrinks down the input beams and causes them to expand, giving us large beams at the transmitter aperture. The second component is the lens f_3, which takes the parallel beams and centers them on the transmitter aperture. Together, these two components take the parallel, collimated beams from the source and creates centered, large beams with different angles at the aperture.

The problem at hand is to choose the lenses and the optical distances such that we get the required w_T and the correct tilt at the transmitter aperture. This design actually only addresses the case in which $d_R/w_R = \alpha_0$, which we assume for simplicity. That is, the image at the receiver aperture is simply a scaled version of the one at the transmitter source, except the beams have a tilt. For this transmitter design, the scaling ratio is given by $(f_2/f_1)/(f_3/L)$, so that

$$w_R = \left(\frac{f_2 L}{f_1 f_3}\right) w_0 \quad \text{and} \quad d_R = \left(\frac{f_2 L}{f_1 f_3}\right) d_0. \tag{3.2}$$

However, the two parts of our design have to be matched together to produce the output we want by picking appropriate optical distances between the lenses. We already know that for the telescope to work, $\ell_1 = f_1 + f_2$, and in order to center the beams, $\ell_3 = f_3$. On the other hand, the distance L_1 between the source focal plane and the first lens is essentially a free parameter; since we typically have $L_1 \ll \pi w_0^2/\lambda$ (as we do in Figure 3-1), variation in L_1 does not have a significant effect anyway.

The main constraint is on ℓ_2. Using Equations 3.1 and 3.2, we find w_T in terms of the design parameters, which after beam propagation and mode-matching, requires

$$\ell_2 = f_2 + f_3 \left[1 + f_3 \left(\frac{1}{L} - \frac{1}{f_4}\right)\right] + \left(\frac{f_2}{f_1}\right)^2 (f_1 - L_1)\,. \tag{3.3}$$

Generally speaking, there exist choices for the lenses (and perhaps L_1) such that Equation 3.3 gives negative values for ℓ_2, which we interpret as meaning the optical setup cannot be solved to implement the focused-beam configuration.

In summary, we should pick lenses f_1 through f_4 (and possibly L_1) such that Equation 3.2 is satisfied and Equation 3.3 has a non-negative solution. For the receiver-side optical design that works with this focused-beam transmitter, see Section 5.1.

3.2 Generating Multiple Spatial Modes

We now finally discuss how we obtain the multiple spatial modes in the first place. If we want to implement FB modes using optical channels, we need to be able to select channels with good isolation, to switch the channels quickly, and to physically arrange the channels in a regular grid pattern. A schematic of the design that implements these requirements is shown in Figure 3-2.

It is convenient to handle this stage of the setup using fiber-based components. There are two major reasons for this: the first is that there is well-developed technology in electro-optic (EO) modulators to perform in-fiber optical switching at high speeds and relatively good isolation. The second is that we can utilize a fiber-coupled microlens array to physically realize the focused-beam configuration. In particular, since our switches utilize polarization, we use polarization-maintaining (PM) fiber.

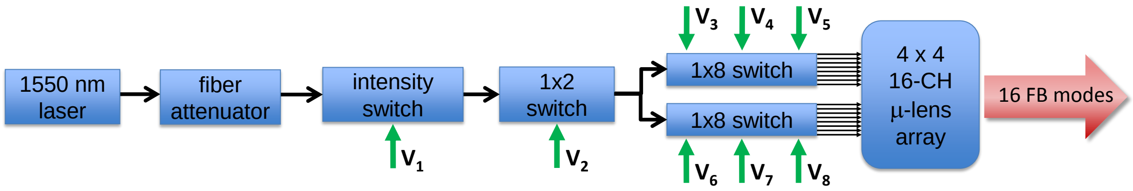

Figure 3-2: Schematic of setup for 16 optical channel focused-beam source Black lines label fiber connections, while the red arrow indicates free-space propagation. Voltage controls to the active switching elements are labeled with vertical green arrows and a voltage. Not shown are the in-fiber isolator and PBS.

Our laser source is a Santec WSL-100 fiber-coupled continuous-wave laser set to output at 1550.116 nm and operating in the 7.00 dBm to 13.00 dBm power range. The laser output is polarized along the key of the PM optical fiber. To prevent back-reflection from our optical elements into the laser cavity and to stabilize the power, we use a Thorlabs PM fiber isolator (PN: IO-G-1550FC).

We attach the output of the isolator to a Thorlabs 50 dB variable PM attenuator (PN: VOA50PM-FC) that allows us to control the output power. For single-photon experiments with nanosecond pulses, around 100 dB of attenuation is sufficient, in which case, two such attenuators can be used in series.

Because our switches require input light polarized along the key of the PM fiber to function correctly, we also add a Thorlabs in-fiber polarization beam splitter (PBS) (PN: PBC1550PM-FC). We use the light coming out of port 1 (aligned to key) and send the light coming out of port 2 (orthogonal to key) into an absorber. In general, port 2 transmits a small but nonzero amount of power (about 0.2%).

The first active optical element in the design is an EOSPACE 10 GHz bandwidth intensity modulator (PN: AX-0K5-10-PFU-UL; SN: 167405) which is controlled by an RF voltage port V_1 in Figure 3-2. The purpose of this switch is to allow us to control the duty cycle of the time modulation, by effectively shutting off the laser except for short bursts to give the spatial modulating components time to change between symbols. Because the experiment has not yet advanced to the stage of using high speed switching, this intensity modulator has not been characterized and is generally not included in any of the experimental setups used for measurements in this thesis.

The second switching element is an EOSPACE 1 × 2 switch (PN: AX-1x2-0K5-20-PFU-PFU; SN: 92320), controlled by an RF voltage port V_2 in Figure 3-2 with switching speeds up to 20 GHz. This switch is used to perform the initial splitting of the laser input into two optical ports, A and B, which are each fed into 1 × 8 switches to produce a total of 16 optical channels. This setup is ideal for a 2-spatial-PPM scheme in which two FB modes are used in each symbol (as in Figure 1-1b); in this case, the 1 × 2 switch acts simply as a beamsplitter, perhaps actively adjusted to account for power imbalances in the 1 × 8 switches. (1-spatial-PPM operation can obviously be done as well.) At this time, the 1 × 2 switch has only been characterized for use in the 2-spatial-PPM mode (see Section 4.2).

It should be noted that, as these two switches are sensitive to temperature fluctuations, they each also have a DC bias port. The V_π voltage to modulate from zero to unit transmission (or from ports A to B in the 1 × 2 switch) only specifies the amplitude for the voltage controls V_1 and V_2; the DC bias to these switches should be determined separately for each individual experiment. (See Section 4.2 for a discussion on this for the 1 × 2 switch.) The DC bias pins used for both switches are pins 1 and 2 (1 for ground and 2 for lead).

The key components in the spatial modulation scheme are the two EOSPACE 1×8 switches (PN: SW-1x2-SP-PFU; SN: 1855-B & 1855-I) that follow. These switches operate up to around 200 MHz and each consists of three voltage controls (labeled in Figure 3-2 as V_3, V_4, V_5 and V_6, V_7, V_8 respectively). The pin numbers used for the six electrical connections on each switch (a lead and ground for each voltage control) are pins 1&5, 10&15, and 18&23. Effectively, each voltage control acts as a 1 × 2 switch layer, three of which are sufficient to split the input light into eight outputs. The output optical ports are labelled B-1 through B-8 and I-1 through I-8, for the serial letter of the switches. Because the switches involve many fiber and electrical connections, we constructed a housing to simplify the setup.

Finally, each optical fiber coming out of the two 1 × 8 switches is coupled into a free-space beam using a microlens array manufactured by Sercalo. The microlens array consists of a precision-machined square array that holds optical fibers in a grid layout, where each fiber tip is fit to a collimating microlens, so the beams come out parallel and well-collimated. The specifications state grid dimensions of 1 mm pitch and 350 µm beam diameter. Experimentally, it is found that the initial focal plane is located about 2 cm from the face of the array, where the waist is $w_0 = 124\,\mu\text{m}$ and the beam separations are $d_0 = 998\,\mu\text{m}$, which fixes a packing ratio of approximately $\alpha_0 = 8.05$ for this entire setup.

The array itself has 28 outputs (a 5 × 5 grid with three additional ports), each served by a single-mode fiber fixed into place by the manufacturer. The 28 fibers come out the back of the array and can be connected to the switch outputs. They have a number associated with them to allow easy identification, and the correspondence between the fiber number and the spatial layout is given in Table 3.1a. It is these dynamically selectable beams coming out of the array which we refer to as the *optical channels*, and we denote them by CH01 though CH16, as shown in Table 3.1b.

24	19	13	20	25
18	**8**	**5**	**9**	**21**
12	**4**	**1**	**2**	**10**
17	**7**	**3**	**6**	**14**
23	**16**	**11**	**15**	**22**
–	26	27	28	–

(a)

CH01	CH02	CH03	CH04
CH05	CH06	CH07	CH08
CH09	CH10	CH11	CH12
CH13	CH14	CH15	CH16

(b)

Table 3.1: Channel layout and designations for free-space array
In 3.1a, we show the spatial layout of the fiber grid on the microlens array and the number of the fiber serving each location, as seen from the front. The bold numbers indicate the 4 × 4 grid we use for the setups in this thesis. In 3.1b, we label this 4 × 4 grid by its corresponding optical channel designations.

The only remaining information we need to specify is the connection scheme between the outputs of the 1 × 8 switches and the microlens array fibers. This determines which switch output goes to which spatial location. A simple scheme, in which outputs B-1 through B-8 couple into CH01 through CH08 (in that order), and I-1 through I-8 into CH09 through CH16, is shown in Table 3.2. However, it is possible to construct a more sophisticated scheme which avoids coupling adjacent channels to switch outputs that share high crosstalk.

Output	Fiber	Channel
B-1	8	CH01
B-2	5	CH02
B-3	9	CH03
B-4	21	CH04
B-5	4	CH05
B-6	1	CH06
B-7	2	CH07
B-8	22	CH08

(a) Switch B connections

Output	Fiber	Channel
I-1	7	CH09
I-2	3	CH10
I-3	6	CH11
I-4	14	CH12
I-5	16	CH13
I-6	11	CH14
I-7	15	CH15
I-8	22	CH16

(b) Switch I connections

Table 3.2: Switch fiber connections to free-space array
This is a simple fiber connection scheme between the switch outputs and the microlens array fibers, together with the corresponding optical channel (see Table 3.1b).

Finally, in order to present a more concrete picture of this schematic outline, we show in Figure 3-3 a photograph of the fiber-based setup implementing the features of this discussion.

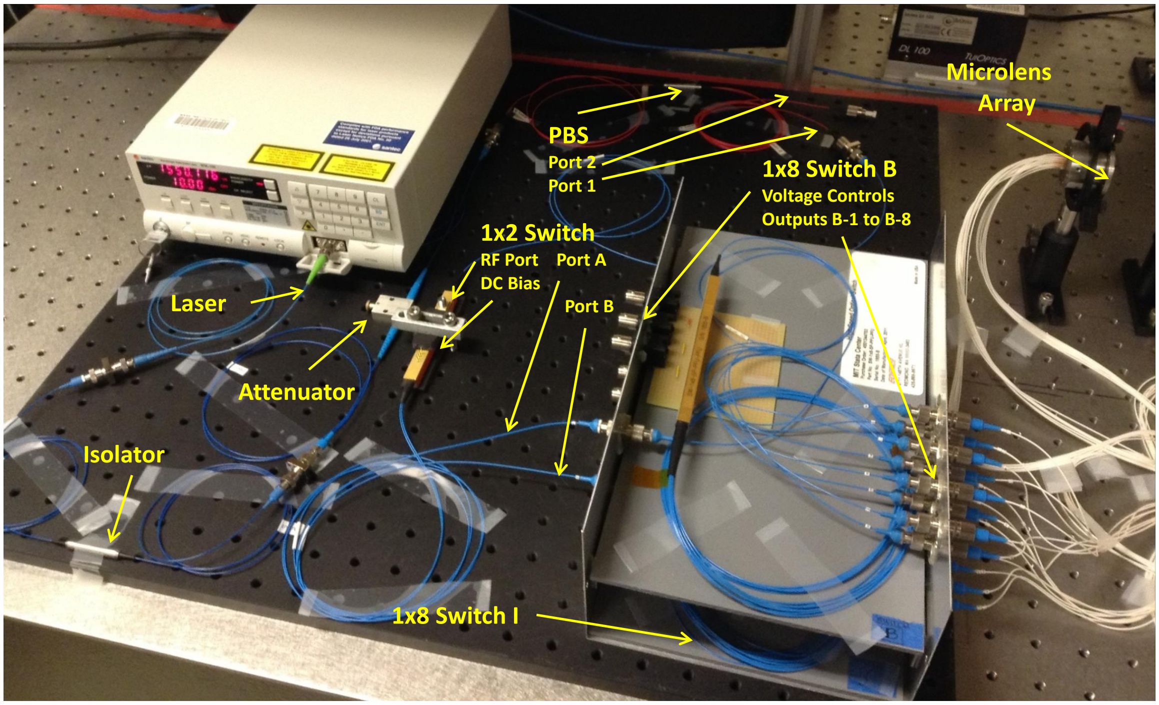
Microlens
Array
PBS
Port 2
Port 1
1x8 Switch B
Voltage Controls
Outputs B-1 to B-8
1x2 Switch
RF Port
Port A
DC Bias
Port B
Laser
Attenuator
Isolator
1x8 Switch I

Figure 3-3: Photograph of lab setup for the multi-spatial-mode source
This photo shows the current setup for generating multiple optical channels using in-fiber switching (blue fibers are PM). Note that the intensity modulator is not included here, and electrical connections are removed to emphasize the optical layout.

3.3 Laboratory Setup for Transmitter Optics

As a check on the optical design for the focused-beam configuration, we build a prototype transmitter setup to verify the propagation of FB modes through our design over laboratory distances. We use the transmitter-receiver designs described in Sections 3.1 and 5.1 to demonstrate that the system behaves as theoretically expected using 16 modes. We describe here the results for the transmitter-side optics; the results for the receiver are discussed in Section 5.2.

We use four lenses as required, all Thorlabs 1-inch diameter, plano-convex lenses with anti-reflection (AR) coating for $\lambda = 1550\,\mathrm{nm}$ light. The lenses have focal lengths of approximately $f_1 = 200\,\mathrm{mm}$, $f_2 = 50\,\mathrm{mm}$, $f_3 = 250\,\mathrm{mm}$, and $f_4 = 200\,\mathrm{mm}$. We also pick $L = 1000\,\mathrm{mm}$ to be a standard laboratory propagation distance between transmitter and receiver. An interesting property of these choices is that, according to Equation 3.2, $w_R = w_0$ at the receiver. Looking at the theoretical simulation in Figure 3-4, it seems that this choice also leads to a constraint on ℓ_2 such that f_3 is placed at a focal plane, which does not happen generally.

According to the simulation, we can choose to set $L_1 = 4.5\,\mathrm{cm}$ and $L = 1000\,\mathrm{mm}$, which together with the specification of the lenses requires $\ell_1 = 25\,\mathrm{cm}$, $\ell_2 = 6.22\,\mathrm{cm}$, and $\ell_3 = 250\,\mathrm{cm}$. This simulation assumes that at the initial focal plane the beams have $w_0 = 124\,\mathrm{\mu m}$ and $d_0 = 998\,\mathrm{\mu m}$, the experimentally confirmed beam dimensions at the initial focal plane.

Of course, we do not know exactly where this initial focal plane lies, just that it is around 2 cm from the face of the array. Furthermore, the focal lengths specified for the lenses are not exact, and the lenses themselves are certainly not thin. As a result, the optical system should be aligned not according to theoretical values but by optimizing various quantities at the appropriate places using a Thorlabs beam profiler (PN: BP109-IR). The positions of the lenses can be tuned very precisely using micrometer translation stages, but the relative values of ℓ_1 and so on are not known to precision. Nevertheless, they should be close, so the theoretical values are a good place to start; only minor corrections should be needed.

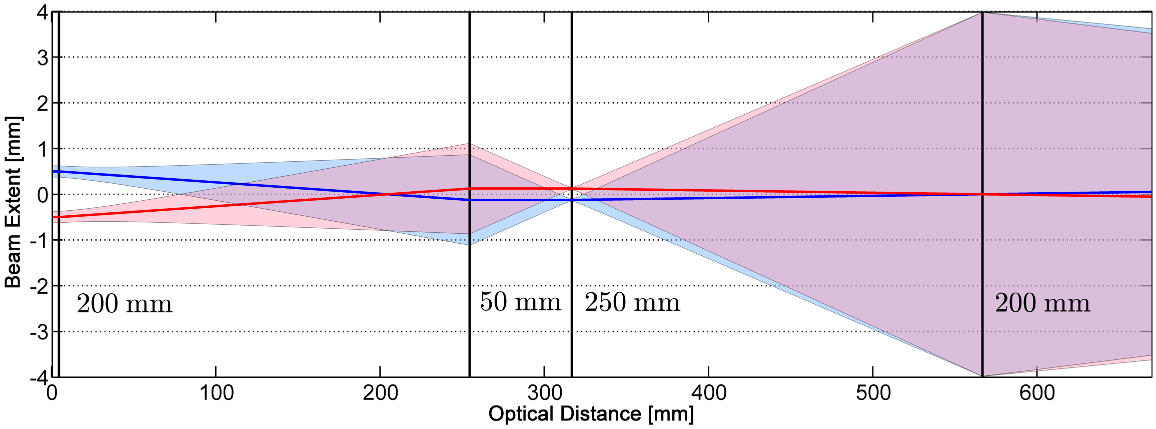

Figure 3-4: Simulation for lab transmitter setup
We show two vertically adjacent FB modes separated by $d_0 = 998\,\mu\text{m}$ with initial beam waists of $w_0 = 124\,\mu\text{m}$ (set by the microlens array) passing through a transmitter setup implementing the schematic in Figure 3-1, with $L_1 = 4.5\,\text{cm}$, $L = 1000\,\text{mm}$, and all other distances chosen as required. We use a thin-lens approximation to the real laboratory lenses, using the focal lengths specified. Note that for this particular choice of dimensions, f_3 is located at a focal plane.

We begin by placing the first lens f_1 about 6 cm from the face of the array, which approximately sets $L_1 = 4.5\,\text{cm}$. This length does not matter significantly since the beams are well-collimated, so there is no need to optimize the position of the first lens. A CCD camera image of the beams at the initial focal plane is shown in Figure 3-5a. This effectively gives an image of the multi-channel output.

The second lens is then placed aproximately 25 cm from the first. To determine the correct location of the second lens, we use a beam scanner to find the focal plane formed by f_2. For a telescope which is exactly tuned, we should find the beam separations at this focus to be $(f_2/f_1)d_0$. We therefore adjust the position of f_2 until this is approximately true. This results in essentially parallel beams, which we also check by moving the beam profiler and observing any relative motion in the centers of the beams. The beam waist at this focus is found to be 31 µm with beam separations 249 µm; the theoretical values are 31.0 µm and 249.5 µm. The CCD camera image at this point is shown in Figure 3-5b.

Coincidentally, this is approximately where we need to place our third lens f_3, as $\ell_2 = 6.22\,\text{cm}$ is where the telescope's focus happens to form. An incorrectly placed f_3 (assuming f_4 is placed correctly a distance $\ell_3 = f_3$ beyond it) results in a focus at the

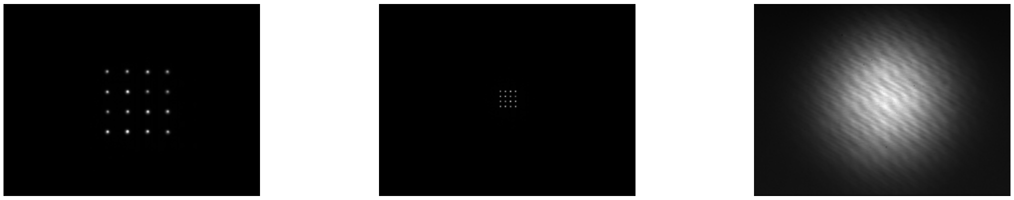

(a) (b) (c)

Figure 3-5: Imaged beam profiles in transmitter optics
The beam profile for the beams is imaged at various points along the transmitter-side optics using a CCD camera. Figure 3-5a is taken at the focal plane of the microlens array; Figure 3-5b at the focus of the telescope's image (also the location of f_3); Figure 3-5c at the transmitter aperture f_4. For Figure 3-5c, however, we use only two channels, CH04 and CH10; nevertheless they overlap.

receiver aperture which is different from L. The idea, then, is to first place f_4 correctly relative to f_3, and then move the two lenses while keeping the relative distance ℓ_3 fixed, until the focus at the receiver aperture occurs approximately a distance L away from the transmitter aperture f_4. We find that ℓ_2 is indeed approximately 6.2 cm. The resulting beams at the receiver aperture have waist $w_R = 125\,\mu\text{m}$ and beam separations of 997 µm, while the theoretical predictions are 124 µm and 998 µm. The CCD camera image at the receiver aperture is shown in Figure 5-3a.

Meanwhile, the location of f_4 itself is actually not critical to the operation of the setup, as the purpose of the lens is simply to cause the beams to begin converging, and the beams are already large at f_4. However, one possible way to check its location would be to use a beam scanner or a CCD camera to determine the location at which the beams are all essentially centered (which is also difficult because the beams are so large). This position for f_4, however, should be found before adjusting the location of f_3, as f_3 and f_4 are moved together. The beams here have a spot size of approximately $w_T = 3.5\,\text{mm}$ and no detectable separations; the theoretical value for the spot size is about 4 mm. A CCD camera image of the large beams at f_4 is shown in Figure 3-5c.

A photograph of the transmitter setup is shown in Figure 3-6. The receiver end is continued and described in Section 5.2.

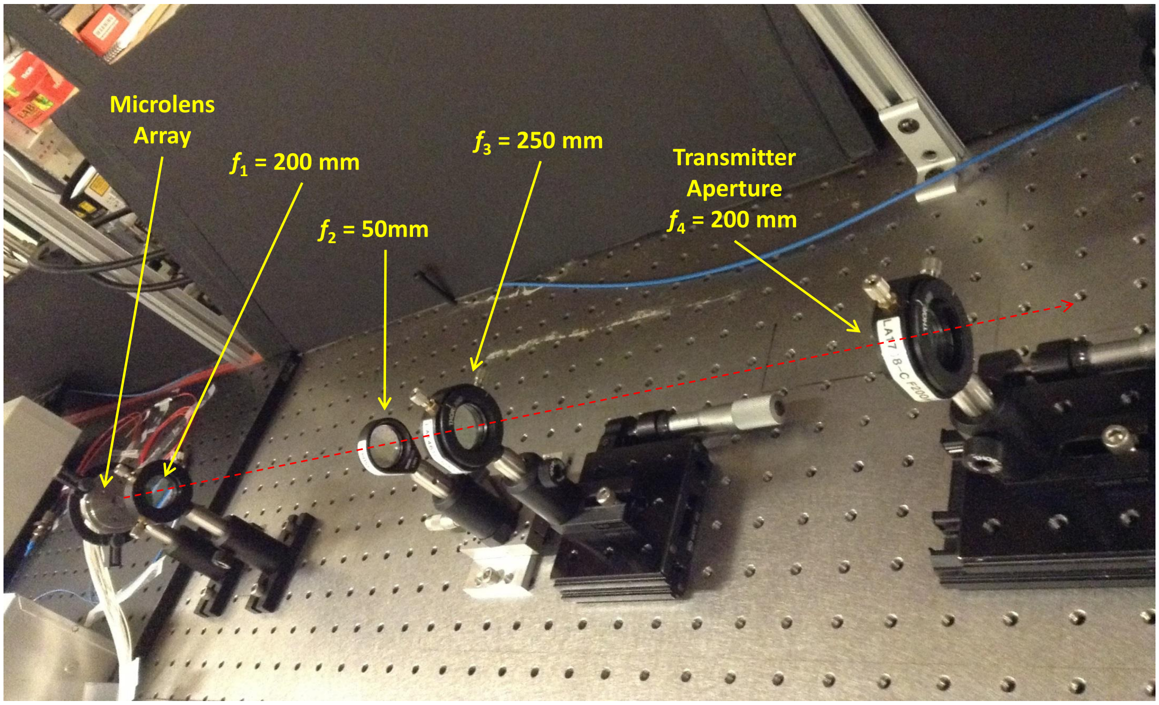
Microlens Array
f_1 = 200 mm
f_2 = 50mm
f_3 = 250 mm
Transmitter Aperture
f_4 = 200 mm

Figure 3-6: Photograph of lab setup for transmitter optical setup

This photo shows the setup for the four-lens transmitter-side design. Lenses f_3 and f_4 are moved together by synchronizing their micrometer readings. Note that no fine-tuning is needed on f_1. The red dashed arrow indicates the direction of propagation along the optical axis.

Chapter 4

Transmitter Interface and Control

Before we discuss the receiver end of the system, we first need to describe the work done in profiling and controlling the optical switches, which is necessary for selecting and for dynamic modulation of the optical channels.

We first find the voltage profiles for the two 1 × 8 switches used in switching between optical channels. We then discuss the use of the 1 × 2 switch to actively adjust power balance. Finally, we briefly describe two National Instruments (NI) LabVIEW programs for achieving static and dynamic control of the optical channels.

4.1 Voltage Profiles for Optical Switching

Recall from Figure 3-2 that the 1 × 8 switches are each controlled by three voltages, either V_3, V_4, V_5 or V_6, V_7, V_8. The voltage profile for a 1 × 8 switch is a list of voltages that, for each optical channel, specifies the three voltages to apply to select that channel. The switches are analog devices, so the distribution of the input light among the outputs varies continuously as the voltages are scanned. However, for each channel, there is one particular set of three voltages which maximizes the output from that channel and hence minimizes the output to all others.

Of course, EOSPACE has provided a list of voltage profiles, in the form of a 16×3 table for each switch. Although these profiles are approximately correct, they are not optimal—deviations of up to 1 V can in fact improve the performance.

As a result, we resort to profiling these switches manually. This is done by scanning the three voltage inputs across a range around the manufacturer-provided ones and optimizing for the maximum optical power going into the selected channel. For each channel, the voltages are scanned using a LabVIEW program which sets (DC) voltages to all three inputs and reads in a single voltage sample from a fiber-coupled photodetector, indicating the relative power going into that channel.

In order for our measurement to work, we assume that the three voltage inputs are uncorrelated. Suppose for example, we pick a channel with optimal voltage settings v_1, v_2, and v_3. Then we assume that even if we fix some suboptimal voltages v_2' and v_3' to the second and third inputs, the maximal power still occurs when the first input is set to v_1. This assumption is reasonable because each of the three voltages controls a different switching layer. As a result, we need only take three scans (or "slices") in order to find the optimal voltages for each channel—we scan one voltage at a time, keeping the other two fixed (e.g., at the center of the range).

For scans around the optimal voltage, the behavior of the switch can be well-approximated by a parabola. We therefore fit a parabola to the data obtained (using the least-squares `polyfit` function in MATLAB) and extract the setting for maximum output. This value becomes the optimal voltage for that scan. A sample of the data obtained and the resulting fits are shown in Figure 4-1. From these fits, we obtain the following voltage profile for the two 1 × 8 switches, as listed in Table 4.1.

Output	V_3 (V)	V_4 (V)	V_5 (V)
B-1	+4.28	+3.29	+3.60
B-2	+4.31	+3.32	−6.40
B-3	+4.31	−6.58	−6.28
B-4	+4.33	−6.66	+3.60
B-5	−5.70	−6.58	+3.81
B-6	−5.80	−6.62	−6.13
B-7	−5.83	+3.20	−6.31
B-8	−5.86	+3.26	+3.54

(a) Switch B voltage profile

Output	V_6 (V)	V_7 (V)	V_8 (V)
I-1	−2.63	−2.05	−2.88
I-2	−2.62	−3.06	+6.63
I-3	−2.62	+6.42	+6.89
I-4	−2.62	+6.44	−2.57
I-5	+6.84	+6.51	−2.66
I-6	+6.81	+6.53	+6.81
I-7	+6.81	−2.94	+6.89
I-8	+6.82	−2.96	−2.55

(b) Switch I voltage profile

Table 4.1: Voltage profiles for 1 × 8 switches

These values are obtained using the slice method of voltage scanning followed by a parabolic fit. Most values are within 1 V of manufacturer's specifications.

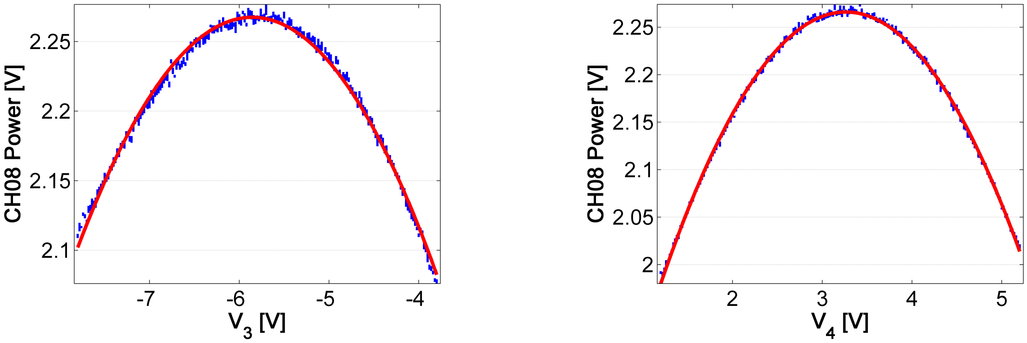

(a) Voltage scan of V_3 (b) Voltage scan of V_4

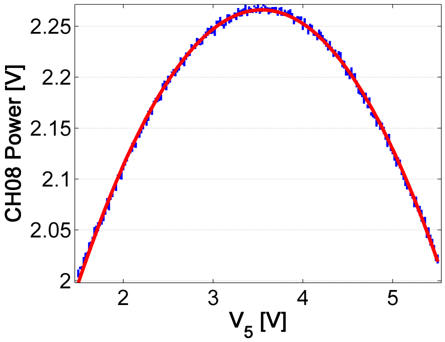

(c) Voltage scan of V_5

Figure 4-1: Voltage profiling fits to voltage scans on 1×8 switch
This is the profiling data for output B-8 (optical channel CH08), recorded using a LabVIEw program. The centers of the scan were $-5.8\,\text{V}$, $3.2\,\text{V}$, and $3.5\,\text{V}$, respectively, with a range on either side of $2\,\text{V}$ and a step size of $0.02\,\text{V}$. Each scan is repeated five times and the results averaged for each point (with the variation represented by error bars). The parabolic fit is shown in red.

4.2 Power Balance and Control

Another aspect of the switches which must be taken into account are the relative transmissivities of the various channels. Because some channels are lossier than others, they do not have the same output power even though the same power is input into the switch; the ratio of the output power of the channel over the input power into the switch is called its *transmissivity*.

For example, in a 2-spatial-PPM scheme, this could cause the top channel to be brighter than the bottom, leading to a malformed symbol. To address the problem, we need to perform modulation on the 1×2 switch—at the same time as our modulation on the 1×8 switches—in order to balance the output power between the two switches.

Of course, after balancing, there may be variation in the power outputs of the various symbols as well, which should be addressed by performing an overall adjustment using the intensity modulator. But because this is not as serious of an issue (having some lossy symbols as opposed to malformed ones), we focus here only on the problem of power balancing for 2-spatial-PPM. To do this, we need to characterize the 1×2 switch and give a scheme for performing the power balancing dynamically.

First, however, we need to obtain the transmissivities of each output on the 1×8 switches. This requirement is easy; we simply apply the voltages found in Table 4.1 and record the ratio between the output and input powers using a fiber-coupled power meter. The results are shown in Table 4.2.

Output	Transmissivity (dB)
B-1	−2.52
B-2	−2.53
B-3	−2.71
B-4	−2.48
B-5	−2.83
B-6	−2.50
B-7	−2.65
B-8	−2.72

(a) Switch B transmissivity

Output	Transmissivity (dB)
I-1	−2.46
I-2	−2.84
I-3	−2.82
I-4	−2.55
I-5	−2.50
I-6	−2.62
I-7	−2.57
I-8	−2.50

(b) Switch I transmissivity

Table 4.2: Channel transmissivity in 1×8 switches
These transmissivities are found using the voltage profiles given in Table 4.1 and expressed in dB. The reciprocal of the transmissivity (its negation in dB) is the insertion loss; these values agree with the specified insertion losses to within 0.3 dB.

We next need to determine a scheme to drive the 1×2 switch for power balancing. As noted in Section 3.2, control of the 1×2 switch requires both a DC bias and an RF port V_2. The idea is to set the DC bias for each experiment such that when the V_2 drive passes through zero, the power is balanced between ports A and B of the switch. Once this is established, the switch's response to small amplitude modulation on V_2 (for example, square pulses in switching between symbols) is approximately linear around 50/50. That is, the ratio R_A of the input power which goes to port A is well-approximated as $R_A = rV_2 + 1/2$, for some slope r (which could possibly depend on drive speed).

Experimentally, it is found that for drives around 10 kHz, we have an approximate value of $r = 0.235\,\mathrm{V}^{-1}$. Suppose now that we wish to perform modulation for a 2-spatial-PPM symbol with unequal transmissivities γ_A and γ_B on the top and bottom, respectively. Then as long as the 1×2 switch is DC biased to 50/50 when the drive passes through zero and the value of r is correct, we can balance the two optical channels by applying

$$V_2 = \frac{1}{r}\left(\frac{\gamma_B}{\gamma_A + \gamma_B} + \frac{1}{2}\right). \tag{4.1}$$

This gives us a "voltage profile" for the 1×2 switch, except that it is specific to the particular 2-spatial-PPM scheme used, including the particular optical connections in going from ports A and B to optical channels. For the scheme described in this thesis, it is a list of 64 voltages to be applied to V_2 simultaneously with V_3 through V_8 on the 1×8 switches, except that instead of being listed according to channel, it is listed according to the 64 symbols. The full list, generated according to Equation 4.1 using $r = 0.235\,\mathrm{V}^{-1}$ and the transmissivities in Table 4.2, is shown in Table 4.3.

Symbol	V_2 (V)	Symbol	V_2 (V)	Symbol	V_2 (V)	Symbol	V_2 (V)
CH(1,1)	+0.013	CH(3,1)	+0.060	CH(5,1)	+0.091	CH(7,1)	+0.045
CH(1,2)	−0.080	CH(3,2)	−0.033	CH(5,2)	−0.003	CH(7,2)	−0.049
CH(1,3)	−0.075	CH(3,3)	−0.028	CH(5,3)	+0.003	CH(7,3)	−0.043
CH(1,4)	−0.007	CH(3,4)	+0.040	CH(5,4)	+0.071	CH(7,4)	−0.025
CH(1,5)	+0.003	CH(3,5)	+0.050	CH(5,5)	+0.081	CH(7,5)	+0.035
CH(1,6)	−0.026	CH(3,6)	+0.021	CH(5,6)	+0.052	CH(7,6)	+0.006
CH(1,7)	−0.013	CH(3,7)	+0.034	CH(5,7)	+0.064	CH(7,7)	+0.018
CH(1,8)	+0.003	CH(3,8)	+0.050	CH(5,8)	+0.081	CH(7,8)	+0.035
CH(2,1)	+0.016	CH(4,1)	+0.005	CH(6,1)	+0.009	CH(8,1)	+0.064
CH(2,2)	−0.077	CH(4,2)	−0.088	CH(6,2)	−0.085	CH(8,2)	−0.030
CH(2,3)	−0.071	CH(4,3)	−0.083	CH(6,3)	−0.079	CH(8,3)	−0.024
CH(2,4)	−0.004	CH(4,4)	−0.015	CH(6,4)	−0.011	CH(8,4)	+0.044
CH(2,5)	+0.006	CH(4,5)	−0.005	CH(6,5)	−0.001	CH(8,5)	+0.054
CH(2,6)	−0.023	CH(4,6)	+0.021	CH(6,6)	−0.030	CH(8,6)	+0.025
CH(2,7)	−0.010	CH(4,7)	−0.021	CH(6,7)	−0.018	CH(8,7)	+0.038
CH(2,8)	+0.006	CH(4,8)	−0.005	CH(6,8)	−0.001	CH(8,8)	+0.054

Table 4.3: Profile for 1×2 switch power balancing

Here, the notation CH(i,j) denotes a 2-spatial-PPM symbol specified by turning on CHi and CH$(8 + j)$, according to the connection scheme described in Table 3.2.

Note that although we have measured r for the typical switching speeds achievable using the NI equipment described in Section 4.3 below, this value can change at much higher speeds. Furthermore, this profile has not been as thoroughly tested as the ones for the 1×8 switches, because up to this point, we either use static switching where setting the DC bias is sufficient, or we do not need exact balance between the top and bottom channels. For these reasons, additional testing of this profile is recommended.

Finally, although we do not give a similar profile for the intensity modulator in normalizing the powers of all the symbols of the 2-spatial-PPM scheme, we do note that it is possible to extrapolate an estimation for the relative intensities of the various symbols by simply looking at Table 4.2. In particular, once the two channels are balanced, the average power going into each should be given by half of $\gamma_A + \gamma_B$. Of course, these values could also be measured directly.

4.3 LabVIEW Interface Programs

The electronic control to the active switching elements is performed using an NI digital-to-analog controller (DAC) PCI card (PN: PCI-6733), capable of up to 1 MSa/s distributed across eight outputs, just enough to drive all the active voltage controls V_1 through V_8. The DAC card is connected to an NI connector block for output to BNC terminals (PN: BNC-2110). The outputs are known internally to the NI system as AO0 through AO7, whose correspondence with the voltage controls is given in Table 4.4. A photograph of the setup with the BNC wiring is shown in Figure 4-2.

NI Output	Control	NI Output	Control	NI Output	Control
AO0	V_1	AO2	V_3	AO3	V_6
AO1	V_2	AO4	V_4	AO5	V_7
–	–	AO6	V_5	AO7	V_8

Table 4.4: Analog BNC connections to switching inputs
This chart details the correspondence between the NI analog output designations and the voltage control ports on the switches. Note that the voltage controls for the 1×8 switches are placed in their own columns (second and third).

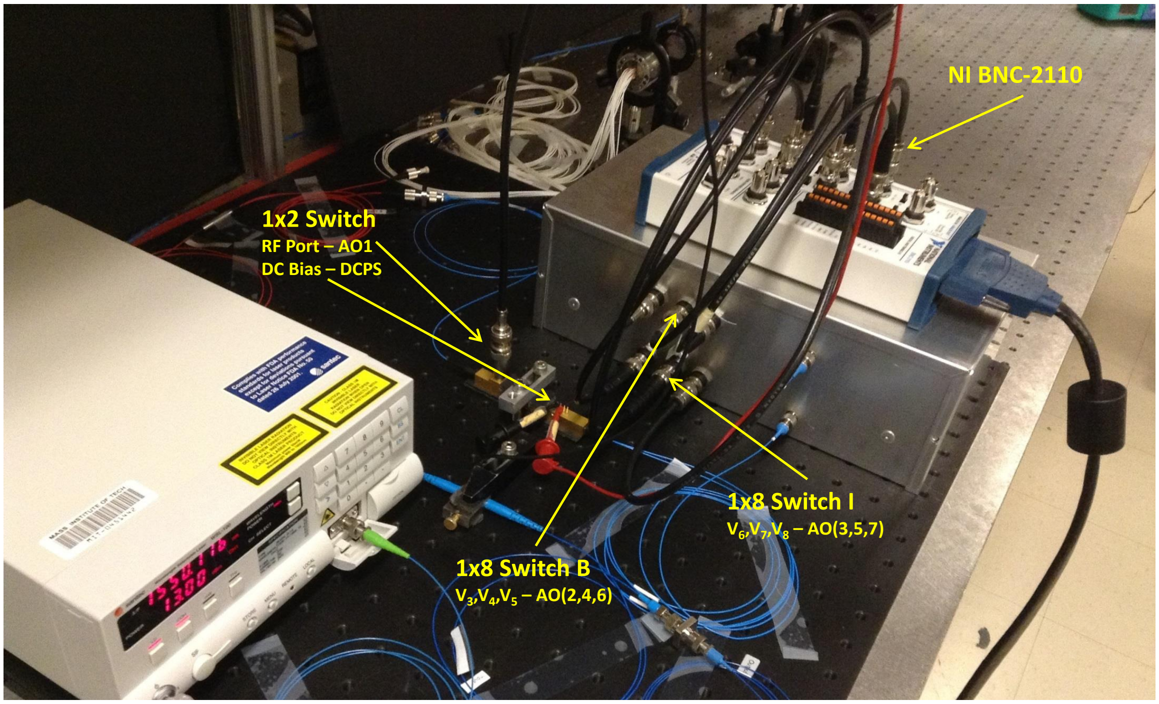

Figure 4-2: Photograph of electronic control setup for active switching
This photograph shows the NI BNC-2110 terminal block resting on the switch housing and its connection to a computer running NI LabVIEW software. The various connections are labelled, with the DC power supply on the 1 × 2 bias indicated by DCPS. Note that AO0 is not used, as the intensity modulator is not included.

The DAC card is controlled via *VI programs* written on the NI LabVIEW programming platform, which provides libraries for IO functionality (called *Data Acquisition* modules or DAQ by NI). Although we will not go into the implementation details, we do provide an overview of the software interface and document some features of its operation. The environment on which these programs have been developed to run is NI LabVIEW 8.5 (licensed for Professional Version) on Windows 7 Enterprise.

The VI program `Double Channel Select.vi` allows manual switching of the 1×8 switches in a 2-spatial-PPM configuration, assuming the optical connection scheme summarized in Table 3.2. The program accepts the specification of voltage profiles in the form of two text files, one for each switch. The format is a white-space-delimited (specifically, three ASCII spaces) 8×3 table of double-format numbers in units of volts. All filenames are with respect to the directory from which the VI program is run. A screenshot of the program interface is shown in Figure 4-3.

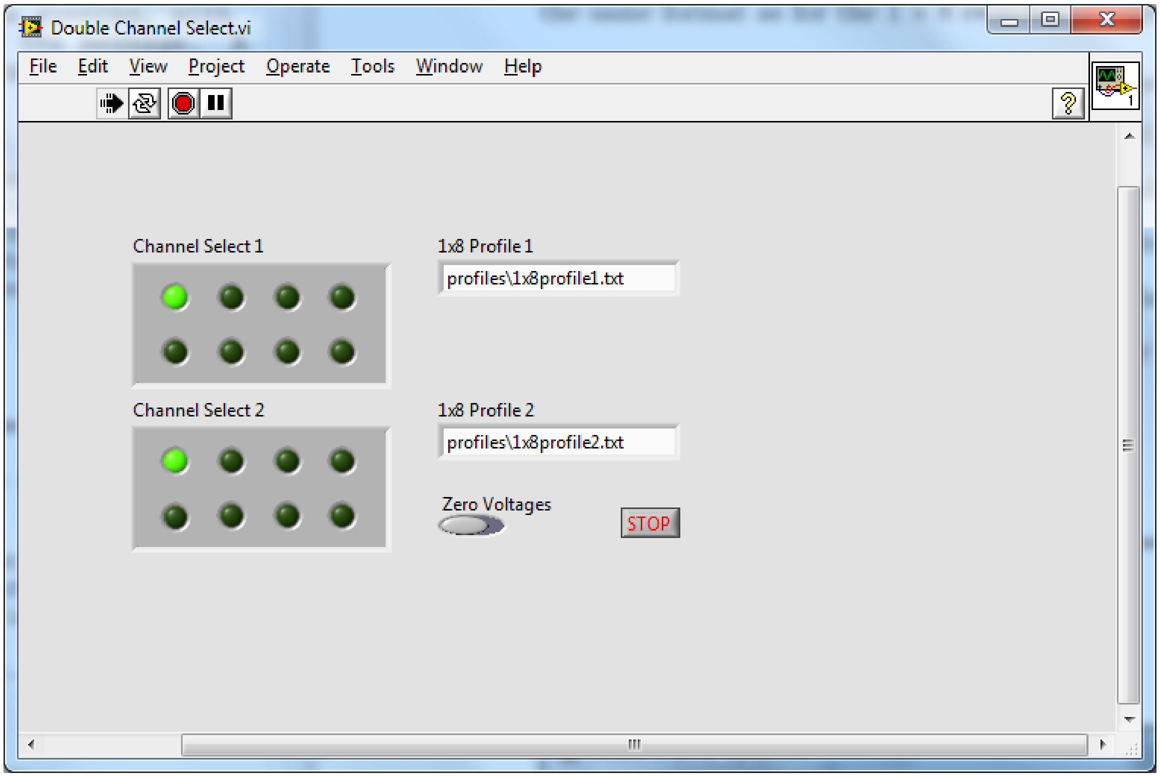

1x8 Profile 1: profiles\1x8profile1.txt

1x8 Profile 2: profiles\1x8profile2.txt

Figure 4-3: Screenshot of `Double Channel Select.vi` interface
A screenshot of a running instance, with the default values for all fields shown, which selects CH(1,1). Note the "Zero Voltages" toggle button is set to the left for channel selection and right for zero. The STOP button terminates the program.

When an optical channel is selected in the interface, the program updates the DC voltage maintained at each of the output terminals by looking up the correct voltages to apply from the profiles. The layout of the channels in the panel follows exactly that of Table 3.1b. A toggle switch is also provided, which sets all outputs to zero.

The second program of interest is `Double Channel Dynamic.vi`, which dynamically drives the switches in order to perform full transmission of a message encoded into 2-spatial-PPM symbols, or pairs CH(i,j) following the notation introduced in Table 4.3. Again, we assume the connection scheme of Table 3.2. The same voltage profiles used for the 1×8 switches in `Double Channel Select.vi` can be used here. However, this program also requires the power-balancing profile for the 1×2 switch, which follows the same format as the 1×8 profiles, except as a 64×1 table.

The message is input as a message file composed of N lines (one for each symbol in the message), each containing two integers between 0 and 7 specifying the codeword.

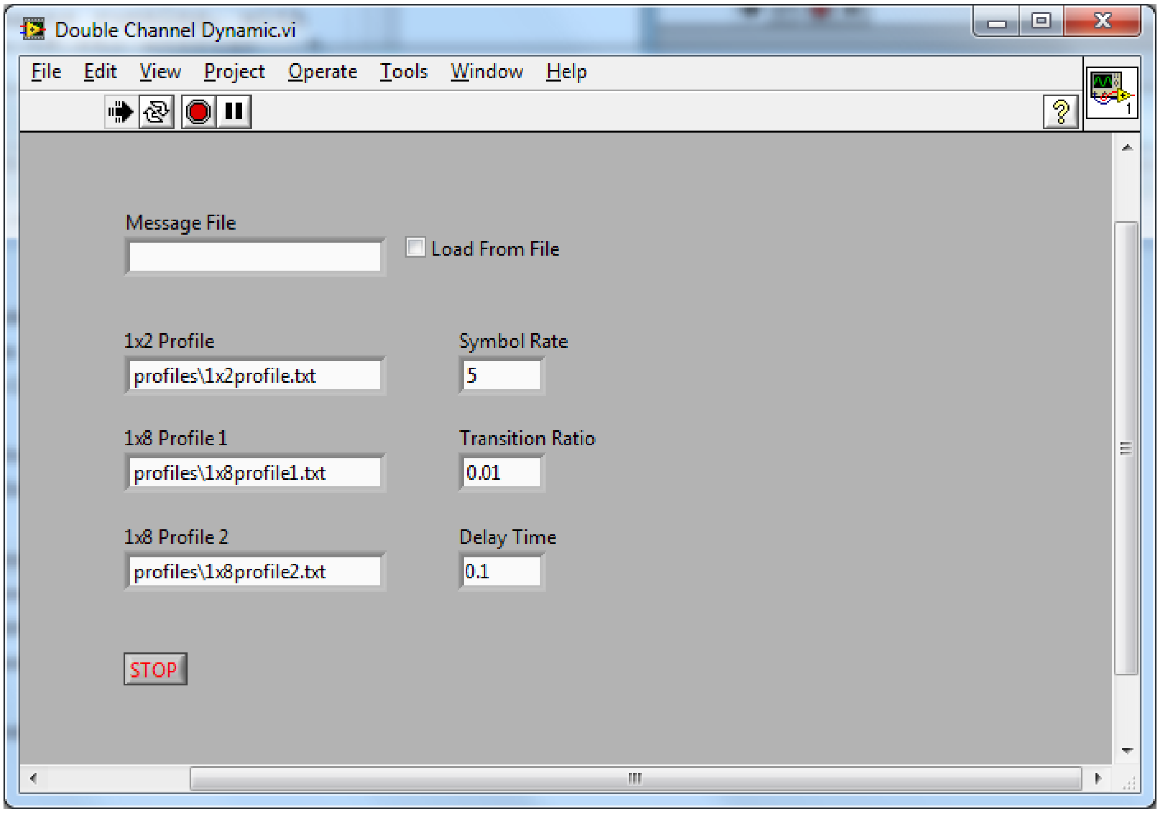

Message File

☐ Load From File

1x2 Profile: profiles\1x2profile.txt

Symbol Rate: 5

1x8 Profile 1: profiles\1x8profile1.txt

Transition Ratio: 0.01

1x8 Profile 2: profiles\1x8profile2.txt

Delay Time: 0.1

Figure 4-4: Screenshot of `Double Channel Dynamic.vi` interface
A screenshot of a running instance, with the default values for all fields shown. Note that file paths are with respect to the directory from which the VI is run. The STOP button terminates the program, though there may be a delay as the current message waveform finishes its output.

For example, we would have the line `4   3` for CH(3,2), setting CH03 and CH10 on. (Note that we again use three ASCII spaces.) The message file is only loaded if the checkbox for “Load from File” is checked. Upon starting up, however, the default behavior of the program is to do a basic scan through all 64 codewords by scanning all CH(i,j), first iterating through j and then i—thus, CH(1,1) is followed by CH(1,2), ending with CH(8,8). In any case, the message is repeated indefinitely as long as the program is running, with a delay time ΔT (in seconds) between each iteration of the message. A screenshot of a running instance of the program is shown in Figure 4-4.

The easiest way to understand the remaining two parameters, the symbol rate f_s and the transition ratio τ, is to examine Figure 4-5, which shows a cartoon rendition of the signal shape which is generated by the program in any one of its outputs.

The symbol rate f_s is the approximate number of symbols sent per second, which need not be an integer. In the figure, we have $f_s = 5\,\text{symb/s}$, which is the programmed default. The transition ratio τ is the ratio between the *rise time* T_{rise} and the signal or *symbol time* T_{symb}, or $\tau = T_{\text{rise}}/T_{\text{symb}}$. The default transition ratio is $\tau = 0.01$.

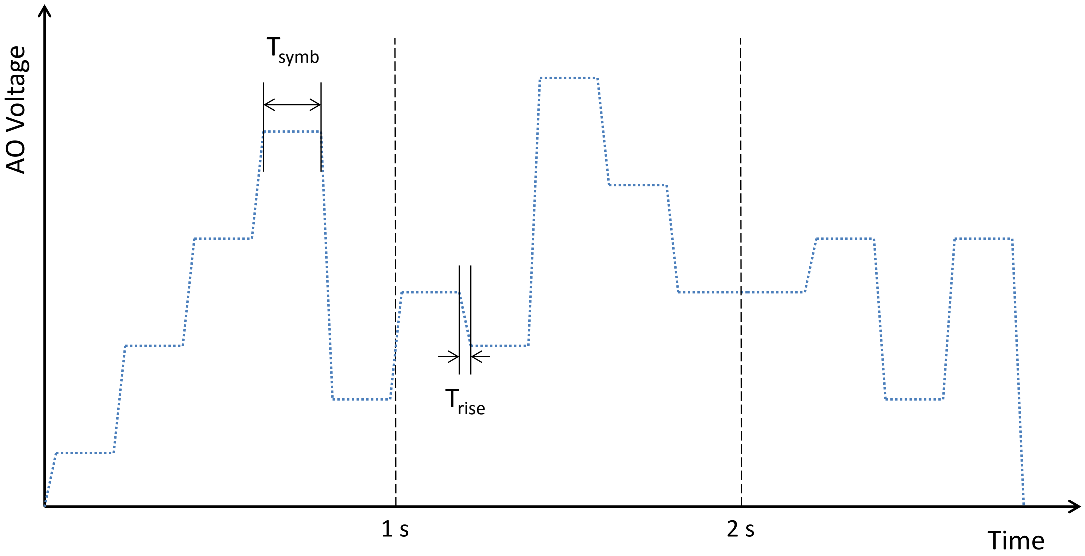

Figure 4-5: Cartoon of dynamic driving waveform for message encoding
This represents the generated waveform used to drive a single iteration of a message on, say, one of the three voltage ports on a 1×8 switch. Here, the voltage profile is idealized to be eight equally spaced levels and all positive. Thus, the various plateaus on the graph represent the selection of particular symbols for a time T_{symb}, with linear interpolation between the values for time T_{rise}. Here, τ has been set to about 0.25. Note that around the 2 s mark, the same voltage is used for two consecutive symbols, and that the voltages begin and end at zero, so no drive is applied during the delay time ΔT. Finally, this waveform is analog but sampled discretely at S Sa/s.

The timing for the waveform is done by relying on the fact that the DAC card outputs a constant number of samples per second S, so by producing a linearly interpolated waveform signal using a vector containing an appropriate number of copies of the voltage sequence, we obtain waveforms of the shape shown in Figure 4-5. An estimate of S used in this program is $S = 124\,085\,\text{Sa/s/ch}$ (samples per second per analog output channel); the total sample rate after factoring in the eight channels is approximately 993 kSa, within the specification of 1 MSa/s. The exact timing of the waveform in implementing the requested f_s depends on how close S is to the actual value; for most applications, this estimate is sufficient.

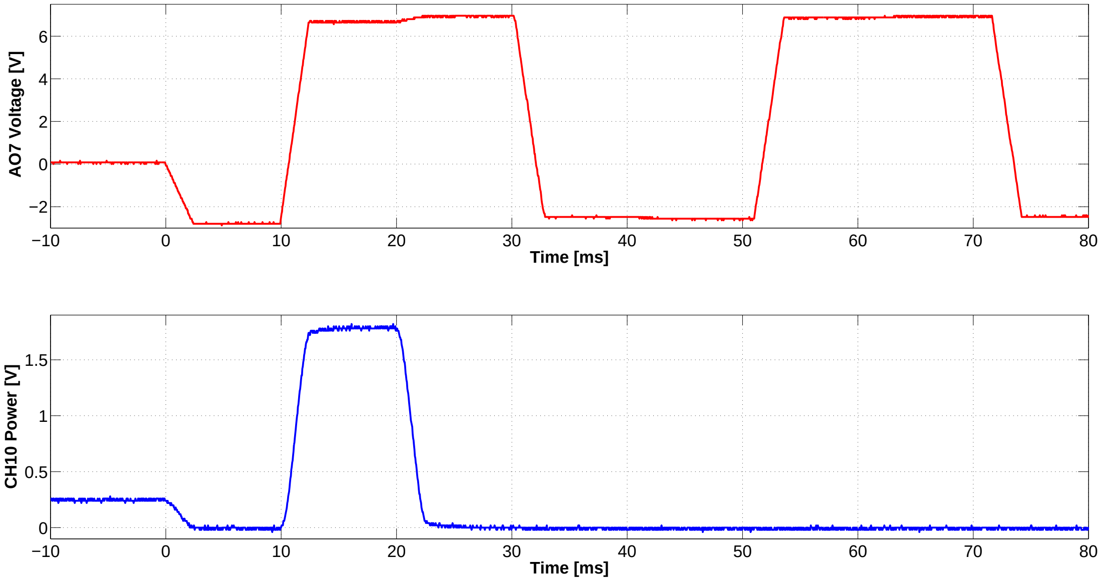

(a) Dynamic driving at $f_s = 100\,\text{symb/s}$, $\tau = 0.3$.

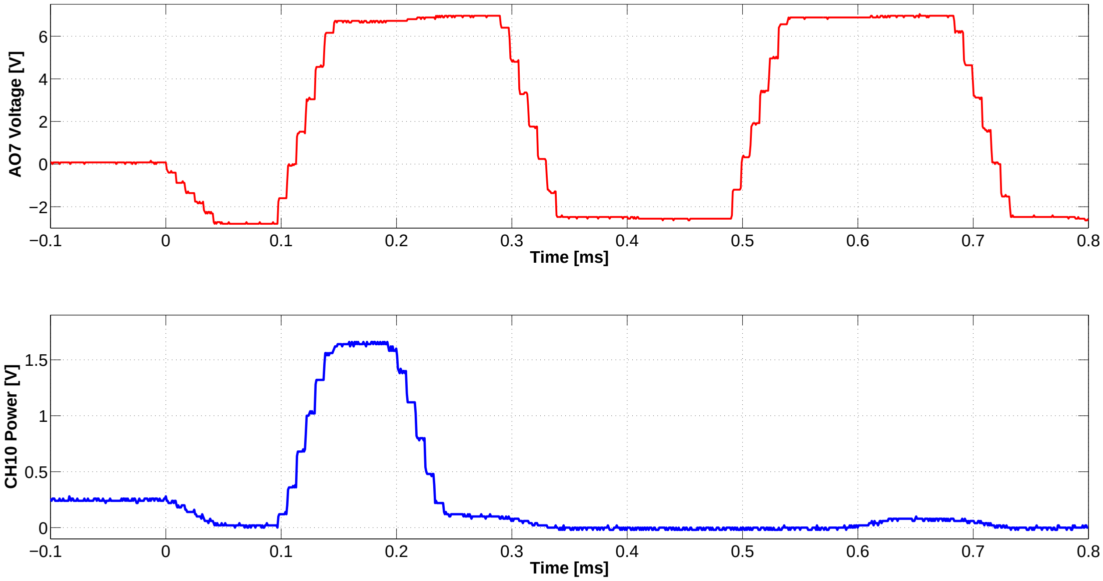

(b) Dynamic driving at $f_s = 10\,\text{ksymb/s}$, $\tau = 0.5$.

Figure 4-6: Voltage waveform and optical response for symbol modulation
We use a scope to record the performance of `Double Channel Dynamic.vi` running the default message at the indicated symbol rates and transition ratios. We monitor AO7 for the driving output, which controls voltage V_8 on switch I, as well as I-2 for the optical output, which controls CH10. The first eight symbols are shown; the rest. are omitted. Note that the program starts correctly at the zero drive state.

In Figure 4-6, we show scope traces of the actual waveform generated by the program on one of its voltage outputs, along with the response of a photodiode monitoring one of the optical channels. In Figure 4-6a, we use $f_s = 100\,\text{symb/s}$ and $\tau = 0.3$, which results in a smooth driving waveform that turns the channel on exactly once over the course of the first eight symbols. There is almost no detectable switch leakage at the level set by the resolution of the scope trace.

In Figure 4-6b, we run the same pattern, except with $f_s = 10\,\text{ksymb/s}$ and $\tau = 0.5$. Now, it is clear that the interpolation is beginning to fail, with obvious jumps made by the waveform as it samples between two voltages. In addition, there is some indication of *optical ringing*, when a channel fails to turn off completely because the switch is driven by discontinuous voltages too quickly. This is evident in switching from the second symbol to the third and on the seventh symbol. None of these effects are seen at the lower rate of 100 symb/s.

Figure 4-7 shows another scope trace also at $f_s = 10\,\text{ksymb/s}$, with an even smaller transition ratio $\tau = 0.1$. At this point, there is nearly no interpolation between the voltage jumps. Again, we see indications of switch leakages that are not present at lower driving speeds.

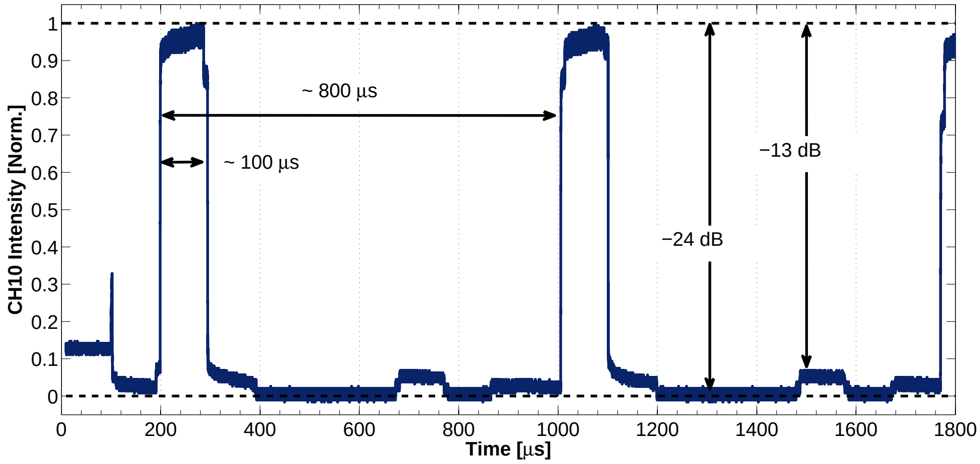

Figure 4-7: Reduced channel isolation at 10 kHz modulation rate
This is the normalized photodiode response monitoring optical output I-2 (CH10), at $f_s = 10\,\text{ksymb/s}$ but with $\tau = 0.1$, giving essentially no interpolation. The trace is annotated with estimations of channel crosstalk using the scope data as well as the timing information. (See Section 6.1 for discussion on channel crosstalk.)

These results indicate that we need alternative options for dynamic control. While the programs have not been tested at symbol modulation rates higher than 10 kHz, a generous estimate on the upper limit given the value of S would be 100 kHz. But as we have seen in this discussion, even at rates approaching 10 kHz, we already run into increased switch leakages. While this problem might be addressable using more sophisticated programming, a full demonstration experiment would require modulation rates on the order of tens to hundreds of MHz, and even higher rates would be needed on the intensity modulator. These requirements are beyond the current capabilities of this NI system.

Chapter 5

Receiver Design and Setup

This chapter describes the receiver design in this experiment. We start by giving the focused-beam receiver optics that collects the FB spatial modes and couples them to a detector array. We complete the discussion on the laboratory realization of the focused-beam configuration optics by showing the receiver-side optics.

While we are on the topic of the receiver, we also go into a brief digression on using single photon superconducting nanowire detector (SNSPD) arrays as free-space single photon detectors, which is necessary in understanding the free-space coupling experiment done in Section 6.4.

5.1 Receiver-side Optics

Recall that using the focused-beam transmitter design in Section 3.1, the beams are focused at the receiver aperture, forming a scaled image of the transmitter source with waist w_R and separation d_R given by Equation 3.2. The beams are also tilted at an angle that depends on d_R and on L.

On the other end, the detector array requires the beams to be once again focused, with beam waist w' and beam separation d', where for simplicity we also assume $d'/w' = \alpha_0$. Now, while it is possible to place a detector immediately at the receiever aperture, it is unlikely that the beam dimensions are appropriate here. Thus, the receiver-side optics, shown in Figure 5-1, are designed to correct the beam by shrinking

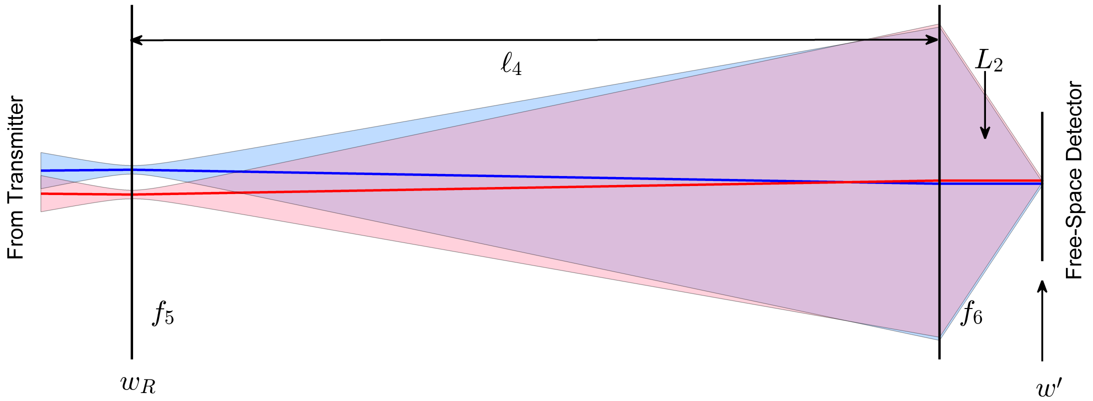

Figure 5-1: Receiver-side optics for the focused-beam configuration
We show the propagation of two FB modes through a two-lens receiver with beam waist w_R at the receiver aperture f_5. The length ℓ_4 is constrained by Equation 5.1 and the length L_2 between the last lens and the detector by Equation 5.2. The beam waist w' at the detector is given by Equation 5.3. This setup combines with Figure 3-1 to implement the focused-beam configuration introduced in Figure 2-2.

it down and setting the rays parallel again.

For this two-lens receiver, the distance ℓ_4 required to bring the rays parallel again can be calculated from geometric optics to be

$$\ell_4 = f_5 + f_6 - \frac{f_5^2}{L - f_5}. \tag{5.1}$$

As with Equation 3.3, this only holds when ℓ_4 is positive; otherwise the system cannot be solved. Because our detector chips are usually small (less than ten microns in width), we utilize tightly focused beams at the detector, which means that f_6 is generally chosen to be small relative to f_5.

After f_6, the beams are parallel and sharply contracting (how sharp depends on how small we make f_6), to form another focal plane at a distance L_2 away, which is where we would place a detector. Using Gaussian beam propagation, we find

$$L_2 = \frac{f_6/f_5}{A^2 + B^2}\left[\left(f_5 - f_6 + \frac{f_6 L}{f_5}\right)A^2 + \left(f_5 + f_6 - \frac{f_5 f_6}{L}\right)B^2\right], \tag{5.2}$$

where $A = \pi w_R^2$ and $B = \lambda L$. In particular, this shows that for $f_5 \gg f_6$ but commensurate with L, we have $L_2 \approx f_6$, as expected.

For this setup, the the beam waist at the focal plane of the detector array is

$$w' = \frac{\lambda w_R}{\sqrt{A^2 + B^2}} \left(\frac{f_6}{f_5} \right) (L - f_5) \, . \tag{5.3}$$

The beam separations can be found using $d' = \alpha_0 w'$ or $d' = (w'/w_0)d_0$. Thus, in summary, the receiver design involves choosing the appropriate lenses f_5 and f_6 such that Equation 5.2 has a non-negative solution and Equation 5.3 yields the correct dimensions to couple with the free-space detector array.

For the transmitter-side optical design that works with this focused-beam receiver to implement the focused-beam configuration, see Section 3.1.

5.2 Laboratory Setup for Receiver Optics

After having implemented the transmitter optics in Section 3.3, we can also verify the the receiver design by building a setup to match the transmitter. Essentially, what we want to show is that not only do we get focused beams after free-space propagation from the transmitter setup, but that we can also then collect the image and modify it as necessary. Of course, we do not utilize a detector array, but simply imaging the beam profiles where the detector would be is sufficient to verify that the optics works and that the result is free of distortions.

We use two Thorlabs lenses, also both AR coated for $\lambda = 1550\,\text{nm}$. The first is a 1-inch doublet with an approximate focal length of $f_5 = 150\,\text{mm}$, while the second is a 1-inch plano-convex lens with focal length $f_6 = 30\,\text{mm}$. A simulation using these two lenses is shown in Figure 5-2, using the input from Figure 3-4.

In order to place the first lens, we recall that in setting the length ℓ_2 in the transmitter optics, we had already optimized the beams to focus at approximately $L = 1000\,\text{mm}$ from the transmitter aperture. Thus, we simply place f_5 at this location in order to form the receiver aperture. As mentioned in Section 3.3, the beams here have waist $w_R = 125\,\mu\text{m}$ and separations $997\,\mu\text{m}$. An image of the beam here is shown in Figure 5-3a.

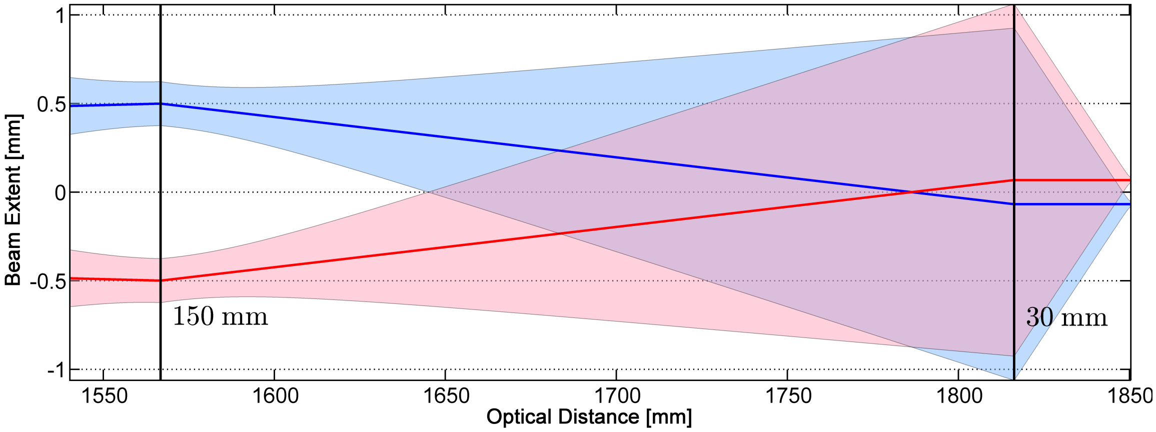

Figure 5-2: Simulation for lab receiver setup
We show two vertically adjacent FB modes propagating through the receiver setup as they arrive from a transmitter setup a distance $L = 1000\,\text{mm}$ away (see Figure 3-4). The beam waist at the receiver aperture is $w_R = 124\,\mu\text{m}$ and separations 998 µm.

We know from our simulation that ℓ_4 should be approximately 20.6 cm, so we place the final lens f_6 near this location. In order to obtain parallel beams, we look for the focal plane and measure α. The location which maximizes the ratio is then the correct position for f_6, while the focal plane is where a detector array would be placed. Here, however, we actually measure $w' = 16.5\,\mu\text{m}$ and $d' = 132\,\mu\text{m}$, while the theoretical values are actually 21.1 µm and 170 µm, which could be due to an inaccurate estimate of the focal length f_5. Nevertheless, this gives $w'/d' = 8.0$, which is very close to the expected $\alpha_0 = 8.05$, so we conclude that the design works as predicted. A CCD image of the beam is shown in Figure 5-3b, but since the beams are too small to be well resolved on the camera, we also provide in Figure 5-4 an image capture from the beam scanner placed near the focal plane.

(a) (b)

Figure 5-3: Imaged beam profiles in receiver optics
The beam profile for a static 2-spatial PPM symbol is imaged at various points along the receiver-side optics. Figure 5-3a is taken at the receiver aperture with a CCD camera, while Figure 5-3b is taken at the detector focal plane.

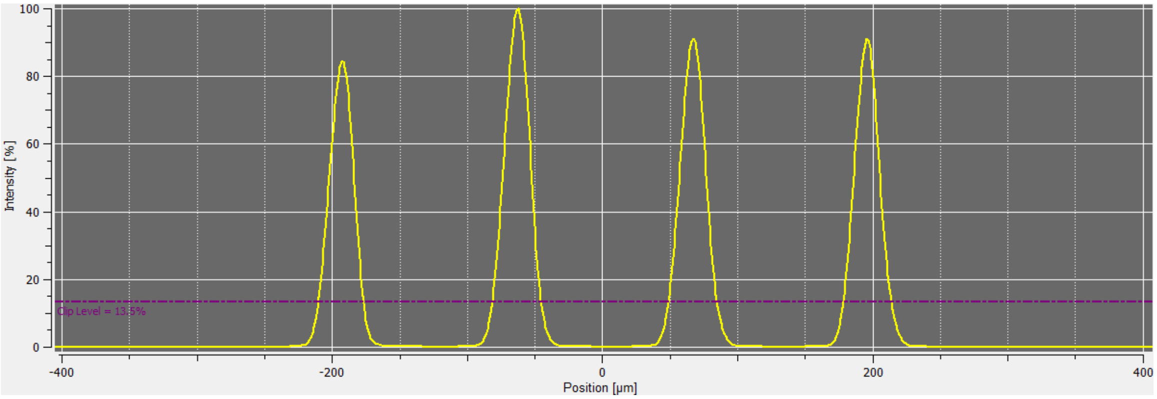

(a) Beam scanner horizontal profile

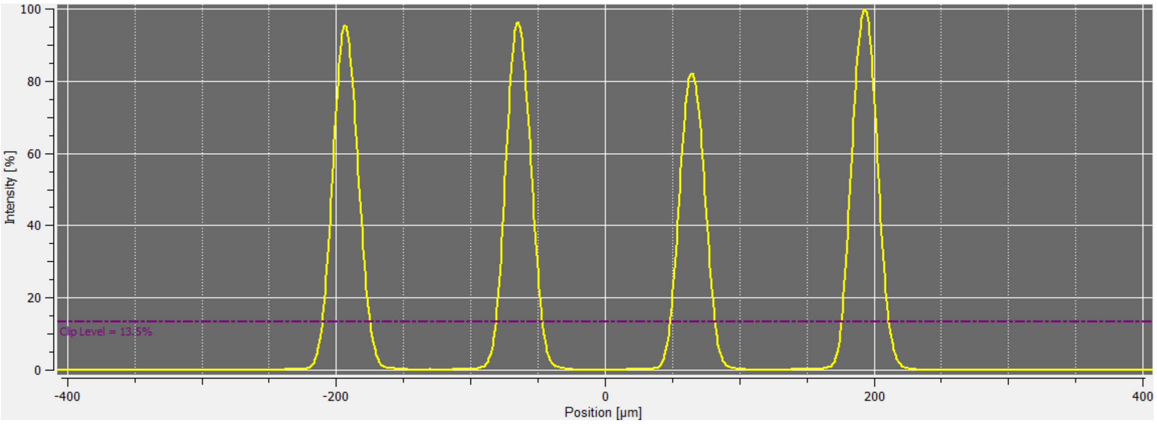

(b) Beam scanner vertical profile

Figure 5-4: Beam scanner profiles at detector focal plane
These profiles are generated by the software for a scanning slit beam profiler at the detector plane, set at 10 Hz scan rate and 1550 nm wavelength input, with all other settings default. All beams are turned on for this profile.

We present in Figure 5-5 a photograph showing the receiver optical setup, including the two mirrors used to fold the optical path in the free-space propagation region between the transmitter and receiver optics.

5.3 Single Photon Free-Space Detectors

While we are on the topic of the receiver, we should also briefly mention some background about *superconducting nanowire single photon detectors* (SNSPDs), which are the type of single photon free-space detectors used in this experiment to perform free-space single photon detection such as in the coupling experiment of Section 6.4.

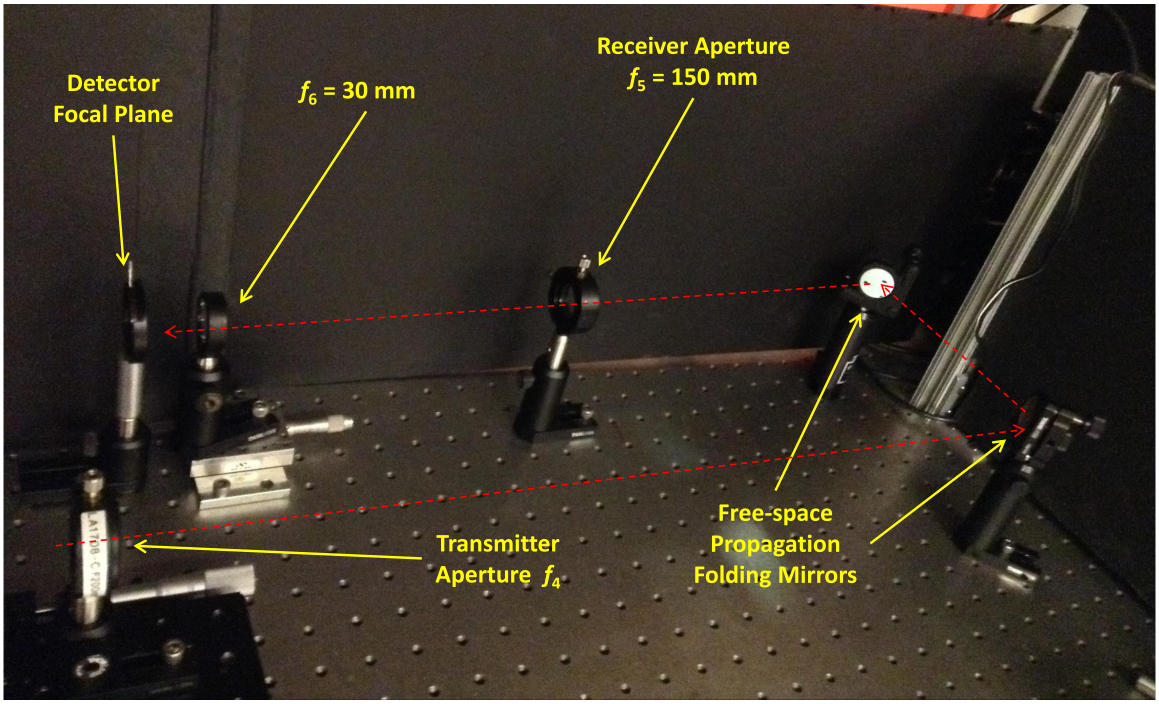

Figure 5-5: Photograph of lab setup for receiver optical setup
This photo shows the setup for the two-lens receiver-side design as well as the free-space propagation region, which is implemented by folding the optical path over with two Thorlabs AR coated mirrors. The red dashed arrow indicates the direction of propagation along the optical axis. An iris is placed near the detector focal plane to indicate its location. Note also the transmitter aperture f_4, shown for reference.

An *SNSPD chip* is a nanofabricated chip which is covered with many windings of a thin superconducting (e.g., NbN) nanowire. When a photon lands on the area of the chip, it is absorbed by the superconducting material, which causes the wire to briefly go out of its superconducting state. This sudden change from a zero resistance state to a resistive one causes a voltage pulse to originate from the nanowire, which can be measured as a "click". In addition to the unique ability to measure the arrival of single photons, SNSPD chips also have the advantage of fast recovery times (on the order of nanoseconds) and low dark count rates (less than kilohertz level). These properties make them useful for high-speed photon counting experiments.

An *SNSPD array* is then just a set of such chips arranged in a grid pattern, with some chip center-to-center distance and chip size. The idea is that the array makes it possible to discern not only *when* a chip fires, but also *which* chip fires, thus allowing photon counting not only in the time domain of arrival time, but also in the spatial domain of arrival location. It is clear that such an SNSPD array would be very useful for single photon FSO with FB modes, provided that we can match the image of the beams with the dimensions of the SNSPD array.

However, the requirements for performing this free-space coupling between a spatial mode source and an SNSPD array is nontrivial, for the reason that SNSPD chips must be placed in thermal and mechanical isolation from its environment in order to achieve superconductivity. The arrays are typically placed inside cryostats, which restricts access to optical elements near the detector, as well as to the detector itself. Thus, light is usually sent through a cryostat window before propagating through the cryostat and hitting the array, making alignment difficult.

In Section 6.4, we perform a series of experiments where the FB spatial modes generated by our transmitter source is sent through a focused-beam configuration to be imaged onto a simple 1×4 SNSPD array, which shows some of these free-space coupling difficulties. The SNSPD array is developed by RLE's Quantum Nanostructures and Nanofabrication (QNN) group [5].

Chapter 6

Characterization of Optical System

We now discuss some results obtained in characterizing aspects of the optical system relevant to performing reliable communication using FB modes. We cannot expect perfect correlation betweeen the message sent out of our encoder and the message found at the decoder; the physical channel necessarily introduces errors. For this communication protocol, these errors occur when light is detected in a spatial mode different from the one intended by the sender.

Of course, when working with high power, small power leakages into other spatial channels can be easily eliminated by *thresholding*, where we interpret only the brightest channel as the intended one. But in single photon OOK direct detection, the arrival of a photon cannot be thresholded—we either get a click in a channel or not—so the probability for error is set by the classical power distribution. Thus, it is important that we characterize the FB modes at all points in the system.

For FB mode channels, the *crosstalk* of an inactive channel j with an active channel i is the ratio between the power in j over the power in i. In some cases, such as at the detector array, this crosstalk is in fact the overlapping and scattering between the individual spatial modes ("spatial crosstalk"). In other cases, such as in the 1×8 switches, it is due to power leakages in an active optical element ("switch crosstalk/leakage"). Knowledge of the channel crosstalk for a particular protocol (like 2-spatial-PPM) allows the design of *error-correction codes* to improve the reliability of the channel by replacing symbols with *codewords* that together have lower crosstalk.

In this chapter, we investigate various aspects of the system which could contribute to channel crosstalk. First, we examine the power leakages in the 1×8 switches, which is essentially where crosstalk is first introduced in our system. Then, we use a CCD camera to look at the spatial crosstalk among the free-space FB modes, which might occur, for example, at the microlens array. Additionally, we can also use the same technique to investigate the spatial crosstalk caused by imperfect focusing of the FB modes, leading them to appear more tightly packed (that is, to have a smaller α).

Finally, we briefly also describe an experiment attempting to couple the FB modes between the transmitter source with a simple 1×4 SNSPD array, which yields insight into the crosstalk issues at the detector side as well.

6.1 Leakages in Active Switching

Let us first consider the channel crosstalk caused by the 1×8 switches. We observe that when we select a single output optical port using our optimized voltage profiles, we still observe a nonzero power in the other ports. Thus, power leaks from the intended output to a different one, which establishes a baseline for the minimum obtainable crosstalk among our free-space FB modes. That is, the channel crosstalk everywhere else in the system can only be as low as the leakages in the switches.

The output leakages on the 1×8 switches are provided by the manufacturer in the form of an 8×8 table for each switch. But because we use our own voltage profiles rather than the manufacturer specified ones, it is a good check to measure the leakages in order to understand the performance of the switches, especially since this is one of the first sources of errors in the system.

The measurement is done by directly fiber-coupling each of the eight output fibers on the switch to a power meter and, for each one, measuring its transmitted power as we step through selecting all eight ports on that switch. This gives us both the power output to each port when it is selected as well as the power output to each port when any of the others are selected. Computing the ratios between each pair of outputs according to the definition of crosstalk gives the results in Table 6.1.

Selected	B-1	B-2	B-3	B-4	B-5	B-6	B-7	B-8
B-1	–	−31.8	−37.2	−33.1	−35.5	−22.4	−34.8	−26.5
B-2	−27.2	–	−30.9	−44.8	−32.7	−22.7	−26.7	−42.6
B-3	−49.1	−29.7	–	−26.7	−32.7	−21.2	−31.8	−40.0
B-4	−27.6	−41.8	−31.8	–	−25.3	−22.8	−31.4	−41.8
B-5	−48.2	−38.8	−30.4	−29.1	–	−21.6	−30.9	−26.9
B-6	−47.4	−39.3	−25.4	−39.1	−28.0	–	−25.4	−39.8
B-7	−48.6	−25.7	−30.6	−38.7	−32.9	−22.7	–	−27.1
B-8	−24.9	−41.9	−30.3	−41.4	−32.6	−22.6	−31.8	–

(a) Switch B leakages (dB)

Selected	I-1	I-2	I-3	I-4	I-5	I-6	I-7	I-8
I-1	–	−37.3	−33.7	−35.3	−33.3	−20.8	−33.3	−34.7
I-2	−28.1	–	−31.8	−42.2	−29.5	−20.7	−31.2	−42.0
I-3	−46.0	−26.4	–	−25.7	−29.7	−20.9	−29.8	−38.8
I-4	−26.9	−39.0	−27.1	–	−32.4	−21.0	−29.8	−42.5
I-5	−49.2	−39.0	−30.1	−28.0	–	−22.2	−31.1	−26.9
I-6	−47.7	−39.1	−26.2	−32.2	−28.6	–	−25.7	−39.8
I-7	−48.3	−28.1	−30.1	−38.6	−30.9	−22.2	–	−28.9
I-8	−27.9	−41.9	−29.9	−42.0	−32.7	−22.0	−31.4	–

(b) Switch I leakages (dB)

Table 6.1: Power leakages in 1 × 8 switches

The row indicates the selected output while the column indicates the output whose crosstalk is presented (in dB). These leakages are found by setting DC voltage controls to the switch according to the voltage profiles in Table 4.1. An attenuation such that the selected ports yield output power around 13 µW is used to ensure no switch heating. The results are consistent with the manufacturer's specifications, including the particularly leaky outputs B-6 and I-6.

We see from these results that—at least in the current scheme—we cannot do any better than around −21 dB of channel crosstalk. Channels B-6 and I-6, which corrspond to CH06 and CH10, are the particularly problematic ones; the power leakage into these channels is almost 0.8% of the selected channel.

Furthermore, as we have discussed in Section 4.3, our NI dynamic driving program also introduces further crosstalk when driven near their limits of around a 10 kHz symbol modulation rate. According to Figure 4-7, this would bring crosstalk to around −13 dB due to optical ringing effects, which is even more problematic than the static leakages of the switch found here.

6.2 CCD Imaging of Spatial Crosstalk

We ultimately want to understand the behavior of the spatial modes as they propagate through the free-space system. For example, we want to be able to capture effects such as light being emitted in the correct source channel but detected in a different receiver channel, due to effects like scattering and optical misalignment, which we generally term spatial crosstalk (as opposed to leakage). We focus on the 2-spatial-PPM scheme of 64 symbols CH(i, j) introduced in Table 4.3.

One particularly simple way we can investigate the spatial crosstalk is by means of an InGaAs CCD camera (Goodrich SU320Hx-1.7RT; SN: 1118S9971), sensitive to light at 1550 nm. Using the camera, we can obtain the beam profile as a two-dimensional image of pixel values, each proportional to the power incident on that pixel. Since the beams are arranged in approximately a 4×4 square grid, we partition the profile into 4×4 superpixels each centered on a beam. These partitions are integrated to estimate the relative power of each beam. As long as these beams are distinguishable as FB modes, the camera essentially acts as a spatial power meter.

In order to obtain accurate results, we first obtain several images of the background when the beams are blocked in order to determine the dark pixel counts of the CCD. The mean of these background images is then subtracted from the image, which is itself averaged over several shots of the same static profile. We focus on capturing the direct output of the microlens array, near (but not exactly at) the focal plane. A typical distance is about 5 cm, which gives $\alpha \approx 6$.

(a) Reference grid

(b) Integration regions

Figure 6-1: Reference grid and integration superpixels for CCD imaging
The image used above are (background-subtracted) superposition of the measurements of all 64 symbols, in order to produce a reference for the relative locations of all 16 FB modes at the CCD plane. The boundaries of the superpixel paritions are shown as white lines (inclusive) in Figure 6-1b, which is otherwise the same image.

To exhibit this idea, Figure 6-1a shows the locations of all the FB modes imaged at the plane of the CCD array, while Figure 6-1b shows the boundaries used for the integrated superpixels. The images in this measurement are 100×100 squares cropped from the CCD image, with superpixel dimensions of 25×25; the centers of the beams are uniform to within one pixel.

In Figure 6-2, we show the image of the symbol CH(6,3) on both a linear and a logarithmic (dB) grayscale. Of particular interest are the power leakages from the switches which can be seen clearly as dim bright spots on the log-scale image in Figure 6-2b, with CH14 being brightest, as expected.

(a) Linear grayscale

(b) Log (dB) grayscale

Figure 6-2: CCD image of symbol CH(6,3) on linear and log grayscale
The image is taken as the average of ten shots of the static profile CH(6,3) profile, from which an averaged background from fifty images is subtracted. For Figure 6-2b, averaged pixel values under one are rounded up to one to ensure the log scale behaves well. The highest pixel value is used in determining the grayscale range.

The analysis of integrating the superpixels after averaging and background subtraction yields a 64×16 list, specifying for each symbol the pixel counts of each superpixel, which provides an estimate for the relative power in each optical channel. The channel crosstalk between any two dim and bright channels is then just the ratio of the two entries. A graphical representation of this data is shown in Figure A-1.

However, we do show the result from one row, again for the symbol CH(6,3), in Figure 6-3. We observe channel crosstalk of -15.5 dB in the worst case between CH07 and CH11 and -20 dB in the best case between CH04 and CH11. This suggests we do in fact see correlation between channel crosstalk and spatial proximity: otherwise dim channels are found to be brighter at a detector by having a spatially adjacent channel lit up, a hallmark of *spatial* crosstalk.

The discrepancy between these results and those of Section 6.1 shows that there

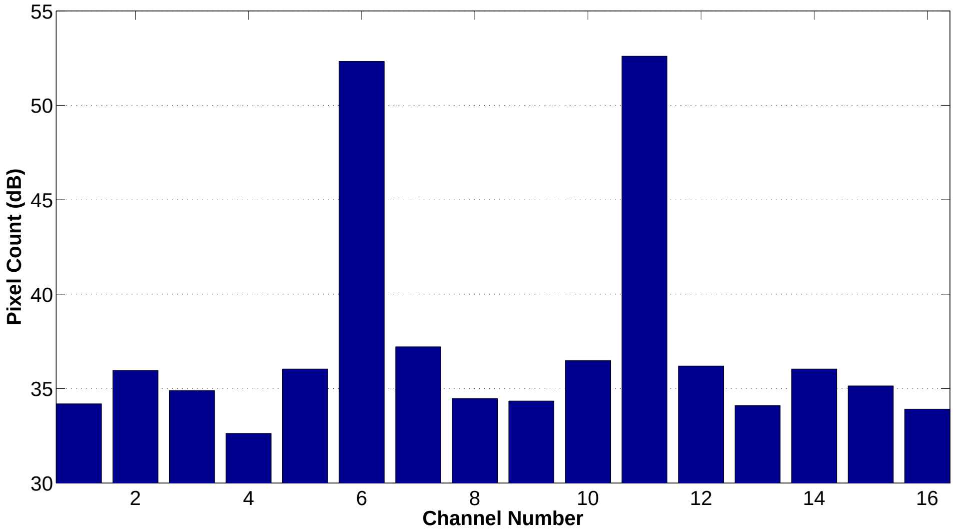

Figure 6-3: Relative channel powers on CH(6,3) by CCD imaging
We show the integrated values of the 16 superpixels on CH(6,3), on a logarithmic (dB) scale. Notice that the baseline is set to 30 dB, and that the two beams are relatively well-balanced. (Balancing was performed manually on the 1 × 2 switch.) Note that these channels are actually arranged a 4 × 4 grid structure, with the two spikes corresponding to the two open channels of 2-spatial-PPM.

there is a general increase in channel crosstalk when the spatial modes are imaged in free-space, extended even beyond adjacent channels. There are several indications that this is the effect of scattering (which can be considered a form of spatial crosstalk). For example, we can compare Figure 6-4a and Figure 6-4b, which shows a group of pixels in the region of the CCD array in which no light from the beams are directly hitting. In the first image, we block off the light from the microlens array and simply measure the mean of the background, while in the second, we let the beams hit the detector array (but not the area in consideration) and again obtain the mean. We see that there is an obvious difference in the pixel intensities. The average pixel value in the first case is 4.6, whereas for the latter, we get around 6.3. This difference implies an essentially diffuse addition to the overall profile, which can impact the integrated pixel counts enough to affect the crosstalk baseline.

It is unclear, however, how much of this is actual scattering at the microlens array when coupling from fiber to free-space, and how much of this occurs at the plane of

(a) Beams blocked

(b) Beams unblocked

Figure 6-4: Diffuse power at CCD array for unblocked beams
These two images are taken from the same 100×100 region of the CCD array, far from any beams. Figure 6-4a shows the averaged background, while Figure 6-4b shows the same region when CH(8,8) is turned on, also averaged (but without background subtraction). The pixels are colored on the grayscale using the maximum pixel value of the right image; it can be observed that the right image is brighter.

the CCD array itself. If the result is due to the scattering at the microlens array, then these measurements are meaningful in that the observed increase in crosstalk is in fact a property of the optical system, which ought to be taken into account. The second case, however, is merely a problem with the measurement using the CCD camera. Nevertheless, this measurement does at least establish a bound on the channel crosstalk that arises due to free-space coupling from fiber at the microlens array, to better than $-14\,\mathrm{dB}$ or so.

6.3 Tight-packing Crosstalk

Although we have already started to see indications of spatial leakages into adjacent channels in Section 6.2, our microlens array still uses a relatively large packing ratio, so the beams are well-separated and distinguishable at the output. However, we can also use the CCD imaging technique in order to investigate the more extreme cases when the FB modes are much closer together. This can be interpreted as either a simulation of the tight-packing regime $\alpha_0 \approx 1$, or, more practically, as what might happen when the beams are imaged or detected outside their focal plane, where the beams are only moderately focused and α is substantially smaller than α_0.

In this setup, we use a defocused telescope with 50 mm and 20 mm lenses, which takes the parallel beams coming out of the microlens array and causes them to converge, while at the same time shrinking the beam waist down so that they expand quickly to a large size not too far from the focus. A sequence of images in which we decrease the value of α at the plane of the CCD array is shown in Figure 6-5.

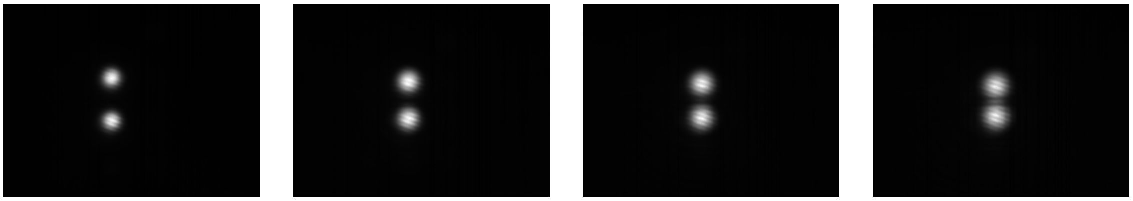
(a) $\alpha = 3.67$ (b) $\alpha = 2.76$ (c) $\alpha = 2.21$ (d) $\alpha = 1.76$

Figure 6-5: FB modes imaged with various α values
We show the image of symbol CH(6,10) as the telescope is defocused, causing the beams to converge closer together at the plane of the CCD array. This gives the approximate values of α indicated above.

We pick a value of $\alpha = 2.71$ to use in repeating the measurements of the relative channel intensities using the CCD camera. The reference grid and the corresponding grid are shown in Figure 6-6. The images in this measurement are 192×192 squares cropped from the CCD image, with superpixel dimensions of 48×48. Note, however, that the beams have a small nonuniform distortion, due to the defocused telescope setup used to achieve the defocusing.

(a) Reference grid (b) Integration regions

Figure 6-6: Grid and superpixels for tight-packed CCD imaging
The image used above are (background-subtracted) superposition of the measurements of all 64 symbols, in order to produce a reference for the relative locations of all 16 FB modes at the CCD plane for the case of $\alpha = 2.71$. Note the small distortions at the edges caused by the optics. However, the beams are still nevertheless well-contained within the superpixel outlines (in white, inclusive).

We can also examine the symbol CH(6,3) in this tight-packing case, which is shown in Figure 6-7, again in both linear and logarithmic grayscale. We see that the beam spot sizes are much closer together, especially as seen on the log-scale image.

(a) Linear grayscale

(b) Log (dB) grayscale

Figure 6-7: Tight-packed symbol CH(6,3) on linear and log grayscale
The image is taken as the average of ten shots of the static profile CH(6,3) profile, from which an averaged background from fifty images is subtracted. For the logscale image, averaged pixel values under one are rounded up to one. The highest pixel value is used in determining the grayscale range.

The same analysis done in Section 6.2 can also be performed here to obtain a 64×16 list of relative pixel counts for each beam (see Figure A-2). We show in Figure 6-8 these integrated pixel counts as a matrix of 4×4 superpixels, colored on a logarithmic (dB) grayscale. Essentially, this is the same representation of the information as with Figure 6-3, but in visual form, which is convenient because it shows quite explicitly the increased spatial crosstalk among adjacent channels that occurs at the CCD array plane, which is the primary effect of tight-packing, or, alternatively, of weakly focused FB modes.

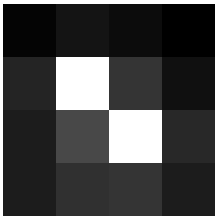

Figure 6-8: Log-scale superpixel matrix for tight-packed symbol CH(6,3)
This image shows the same information as in Figure 6-3, but in a visual layout respecting the spatial arrangement of the optical channels. The image is colored in logarithmic (dB) scale, with the highest superpixel used in determining the grayscale range. Note the spatial crosstalk among adjacent channels.

6.4 Free-space Coupling Experiment

We discuss the results of a collaborative free-space coupling experiment done using the transmitter system described in this thesis with a 1 × 4 SNSPD array developed and maintained by the QNN group at RLE. A discussion about using SNSPD arrays for single photon free-space detectors for FB modes is given in Section 5.3.

While this experiment does not attempt to perform any message encoding or symbol modulation, it does aim to test whether the different optical channels output by the transmitter source can be coupled effectively through free-space optics to the detector channels of an SNSPD array. Furthermore, the experiment utilizes a low-power picosecond laser (PicoQuant) as the input to multiple channel source, which allows the SNSPD to operate in the single-photon regime. The goal, then, is to observe counts in the detector channel corresponding to the selected transmitter channel.

In order to evaluate the quality of the coupling, we need a way to distinguish clicks from different chips, as well as a way to determine which source channel the photon originated from. The chips on the SNSPD array are designed to output a unique differential voltage (500 mV, 250 mV, −250 mV, and −500 mV), allowing the clicks in each detector to be distinguished by histogramming of the voltage signal.

Furthermore, we put a delay line on each source channel (0 ns, 5 ns, 10 ns, and 15 ns), so that by histogramming the arrival time of the photons, we can distinguish the source channel as well. This latter modification is essentially repetitively encoding the transmitted information into both space (using spatial-PPM) and time (using time-PPM), and using the latter to evaluate the former.

The free-space optics utilizes the full FB configuration, except that a three-lens receiver is used instead of the two-lens design described in Section 3.1. After passing through the free-space optics, the beams enter a cryostat in which the detector array is placed. We utilize switch B to perform the active switching, using outputs B-6 (0 ns delay), B-1 (5 ns delay), B-4 (10 ns delay), and B-5 (15 ns delay).

The results of the coupling experiment, shown as a two-dimensional matrix in histogrammed delay time and differential voltage signal, are shown in Figure 6-9.

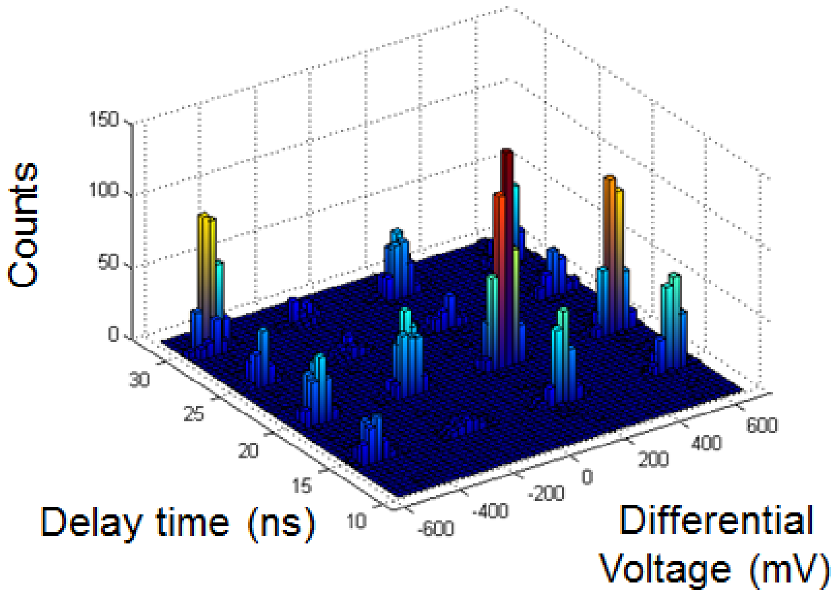

Figure 6-9: Source-detector channel correlations in free-space coupling
This figure is adapted from a report by the QNN group, showing the correlations between detected photons with various delays (representing the source channel) and the differential voltage triggered at the detector (representing the detector channel).

The results are of course far from optimal. While there is some indication of correlation, particularly with the first and last channels, the other channels are distributed rather evenly, which suggests that the beams are not focused effectively onto the detector array, leading to some channels effectively "flooding" the entire detector array rather than being focused down onto a single chip. This result indicates that there is work to be done at the detector end of the system in making the coupling through a cryostat with tightly focused beams easier and less prone to trial and error.

Chapter 7

Conclusions

With regards to the experimental goals outlined in Section 1.3, the work in this thesis has addressed the first three requirements in design, characterization, and control by considering actual implementations currently available and assessing their suitability for a proof-of-concept demonstration of efficient, multi-spatial-mode FSO.

On the transmitter side of the design, we currently have the capability to deliver up to 16 spatial modes using just active switching and a microlens array. In scaling up this number, however, it is likely that we will encounter difficulties in the sizes of microlens arrays available and the complexity involved in adding more fiber-based switches. For hundreds of spatial modes, it is certain that we will need to augment the spatial mode generation with alternatives such as digital micromirror devices.

We also noted in this thesis, particularly in Chapter 6, that in characterizing the optical system, we find the switch crosstalk is rather high, in some cases greater than $-15\,\mathrm{dB}$. This presents problems for error-correction codes, many of which require around $-50\,\mathrm{dB}$. This may only be achievable through the use of additional control elements such as optical shutters to further reduce the crosstalk among the optical channels. Crosstalk at the detector still remains fairly unexplored, and it is possible that the difficulties encountered in Section 6.4 may arise in a future attempt.

For control, the current system using NI DAC cards is sufficient for static or slow modulation, but for practical communication, alternatives such as FPGA controls might be necessary to allow faster performance.

It is hoped that these assessments and characterizations will be helpful in directing future work on this project towards more scalable, efficient designs capable of demonstrating the feasility of efficient multi-spatial-mode FSO.

Appendix A

CCD Camera Crosstalk Data

This page left intentionally blank. See next page.

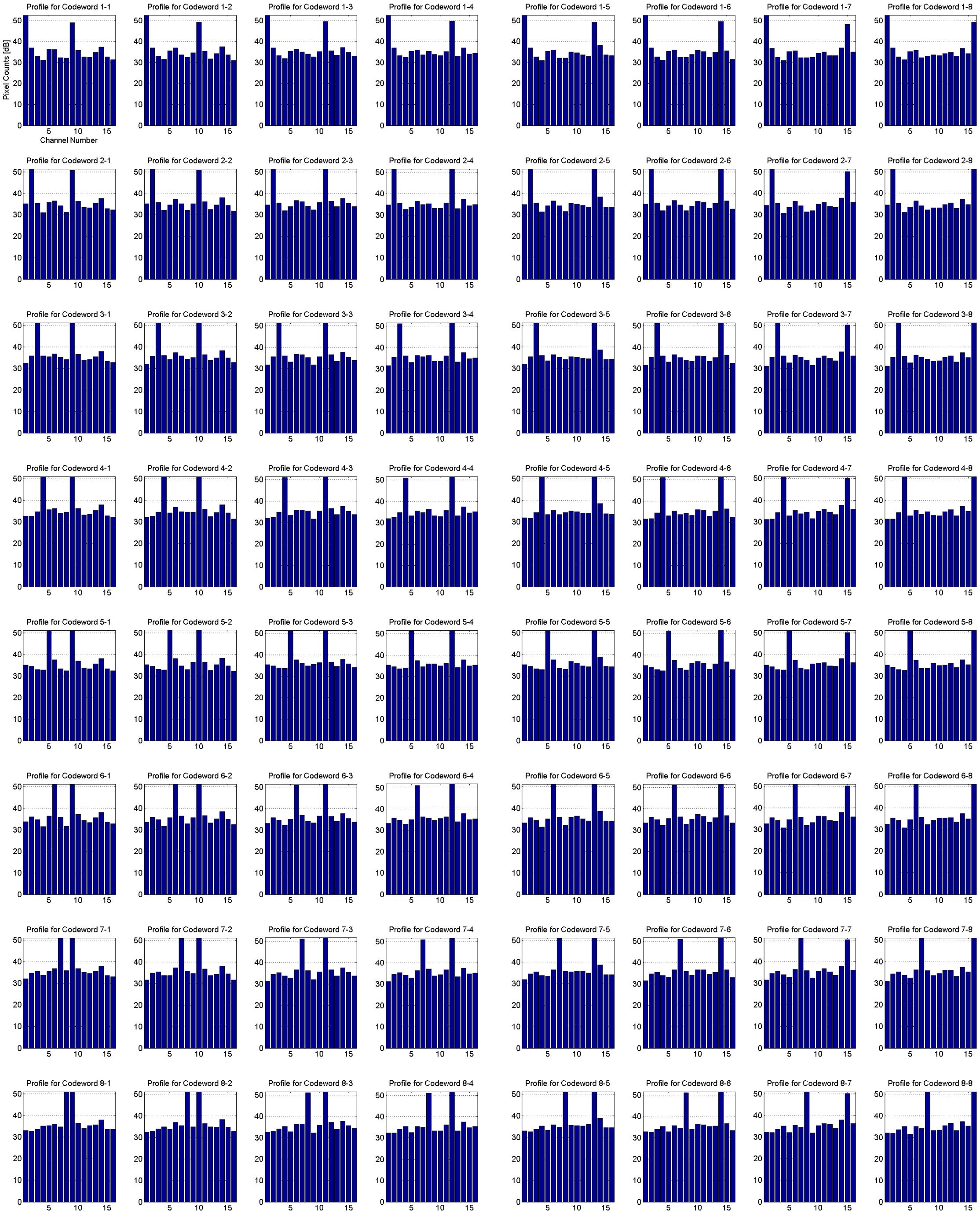

Figure A-1: CCD imaged channel crosstalk data, at microlens array
These are all the channel crosstalk data referenced in Section 6.2, expressed in terms of the integrated pixel values of each channel and given in dB.

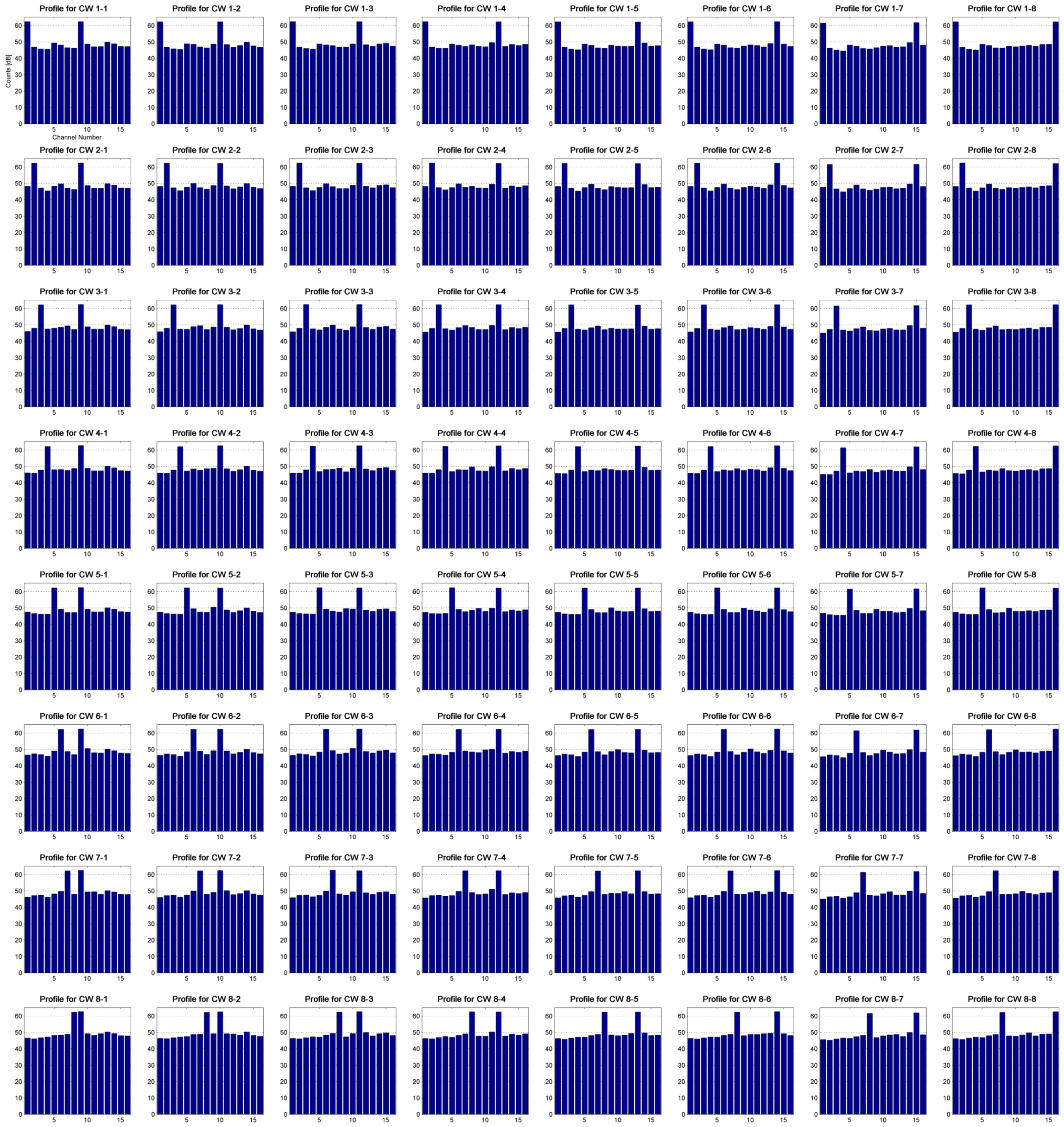

Figure A-2: CCD imaged channel crosstalk data, tight-packing
These are all the channel crosstalk data referenced in Section 6.3, expressed in terms of the integrated pixel values of each channel and given in dB.

Bibliography

[1] S. Guha, Z. Dutton, and J.H. Shapiro, "On quantum limit of optical communications: concatenated codes and joint detection receivers", *2011 IEEE ISIT Proceedings*, pp. 274–278 (2011).

[2] N. Chandrasekaran, J.H. Shapiro, and L. Wang, "Photon information efficient communication through atmospheric turbulence", *Proceedings of SPIE* **8518**, 851808 (2012).

[3] A.E. Siegman, *Lasers*, Ch. 15 & 17, University Science Books (1986).

[4] H. Kogelnik and T. Li, "Laser Beams and Resonators," *Applied Optics* **5**, pp. 1550–1567 (1966).

[5] Q. Zhao, A. McCaughan, F. Bellei, F. Najafi, D.D. Fazio, A. Dane, Y. Ivry, and K.K. Berggren, "Superconducting-nanowire single-photon-detector array," Unpublished manuscript in progress (2013).